Interactive Soil Dust Aerosol Model in the GISS GCM. Part I: Sensitivity of the Soil Dust Cycle to Radiative Properties of Soil Dust Aerosols

Jan Perlwitz[1],

Department of Applied Physics and Applied Mathematics, Columbia University in The City of New York, New York

Ina Tegen,

Max Planck Institute for Biogeochemistry, Jena, Germany

Ron L. Miller,

NASA Goddard Institute for Space Studies, New York, New York

Short title: INTERACTIVE SOIL DUST MODEL. DUST CYCLE

Abstract.

The sensitivity of the soil dust aerosol cycle to the radiative forcing by soil dust aerosols is studied. Four experiments with the NASA/GISS atmospheric general circulation model, which includes a soil dust aerosol model, are compared, all using a prescribed climatological sea surface temperature as lower boundary condition. In one experiment, dust is included as dynamic tracer only (without interacting with radiation), whereas dust interacts with radiation in the other simulations. Although the single scattering albedo of dust particles is prescribed to be globally uniform in the experiments with radiatively active dust, a different single scattering albedo is used in those experiments to estimate whether regional variations in dust optical properties, corresponding to variations in mineralogical composition among different source regions, are important for the soil dust cycle and the climate state. On a global scale, the radiative forcing by dust generally causes a reduction in the atmospheric dust load corresponding to a decreased dust source flux. That is, there is a negative feedback in the climate system due to the radiative effect of dust. The dust source flux and its changes were analyzed in more detail for the main dust source regions. This analysis shows that the reduction varies both with the season and with the single scattering albedo of the dust particles. By examining the correlation with the surface wind, it was found that the dust emission from the Saharan/Sahelian source region and from the Arabian peninsula, along with the sensitivity of the emission to the single scattering albedo of dust particles, are related to large scale circulation patterns, in particular to the trade winds during Northern Hemisphere winter and to the Indian monsoon

circulation during summer. In the other regions, such relations to the large scale circulation were not found. There, the dependence of dust deflation to radiative forcing by dust particles is probably dominated by physical processes with short time scales. The experiments show that dust radiative forcing can lead to significant changes both in the soil dust cycle and in the climate state. To estimate dust concentration and radiative forcing by dust more accurately, dust size distributions and dust single scattering albedo in the model should be a function of the source region, because dust concentration and climate response to dust radiative forcing are sensitive to dust radiative parameters.

1. Introduction

The effect of tropospheric aerosols on the global climate via direct or indirect radiative forcing is one of the largest uncertainties in climate change studies [*Shine and de F. Forster*, 1999]. Among these aerosols, soil dust is a potentially important climate forcing factor due to its high optical thickness: 30% of the aerosol optical thickness is estimated to be caused by soil dust aerosols; roughly half of the current atmospheric dust load is estimated to be anthropogenic in origin [*Tegen and Fung*, 1995; *Tegen et al.*, 1996]. Although the highest dust concentrations are found over land, observations by direct measurements [*Prospero*, 1996], satellite retrievals [*Moulin et al.*, 1997; *Herman et al.*, 1997; *Husar et al.*, 1997], and model experiments [*Tegen and Fung*, 1994, 1995] have revealed that a dust plume can extend thousands of kilometers offshore in certain regions. Dust aerosols dominate the light scattering downwind of the dust source regions [*Tegen and Lacis*, 1996; *Li et al.*, 1996]. For example, *Alpert et al.* [1998] estimated that at 30 dusty days per year, the presence of dust leads to a heating rate of about 6 K per year in the lower atmosphere over the eastern tropical North Atlantic Ocean. In addition to its radiative effect, soil dust may also impact atmospheric chemistry by providing surfaces for heterogeneous chemical reactions [*Dentener et al.*, 1996; *Tabazadeh et al.*, 1998].

The soil dust cycle has been studied using off-line transport models to test source and sink parameterizations of soil dust [*Wefers and Jaenicke*, 1990; *Tegen and Fung*, 1995; *Marticorena and Bergametti*, 1996; *Schulz et al.*, 1998]. Other studies include

dust as a tracer in a general circulation model (GCM) [*Joussaume*, 1990; *Genthon*, 1992; *Tegen and Miller*, 1998], the former mainly to simulate dust distributions under paleoclimate conditions. However, those studies did not include the radiative effect of dust on climate dynamics. The climate response to dust forcing has been addressed in only very few studies so far [*Coakley and Cess*, 1985; *Miller and Tegen*, 1998]. However, those studies used prescribed dust distributions that could not be modified by changes in the soil dust cycle caused by the model dynamics. Other studies emphasized the great uncertainty of the radiative forcing by dust due to its sensitivity to radiative parameters such as single scattering albedo [*Liao and Seinfeld*, 1998; *Claquin et al.*, 1998; *Sokolik and Toon*, 1999; *Miller and Tegen*, 1999].

In this paper, we present new results of our work to assess the climate impact of soil dust aerosols using the National Aeronautics and Space Administration/Goddard Institute for Space Studies (NASA/GISS) atmospheric GCM (AGCM). There are two predecessor studies [*Tegen and Miller*, 1998; *Miller and Tegen*, 1998] which are continued here. In *Tegen and Miller* [1998] soil dust was included as a dynamic tracer, but the radiative effect of dust was not taken into consideration. In *Miller and Tegen* [1998] the radiative effect was examined using a prescribed soil dust aerosol distribution. In the current study, both approaches are combined. In the GISS AGCM, soil dust is included as a dynamic tracer whose distribution is a function of various climate variables. Radiative forcing by dust changes the climate variables in the model such as the surface wind and rainfall, which in turn influence dust emission, transport, and deposition. That is, the soil dust aerosol model is fully coupled with the other climate

variables in the AGCM.

Dust optical properties should vary with the mineralogical composition of the source region. However, for simplicity, and to minimize the computational burden, we assign the optical properties of all source regions using measurements of far-traveled Saharan dust according to *Tegen and Lacis* [1996]. Because the top of atmosphere (TOA) radiative forcing of Saharan dust is coincidentally poised between heating and cooling of the column [*Miller and Tegen*, 1999], our choice may underestimate the effect of dust on climate. Thus we carried out sensitivity experiments with varying radiative properties of the dust particles, represented by the single scattering albedo ϖ of dust. The sensitivity of our results to single scattering albedo will indicate the importance of parameterizing the optical properties of each dust source region separately. In this paper, the analysis emphasizes the modifications of the soil dust aerosol cycle due to radiative forcing by dust, as well as its sensitivity to the radiative properties of the dust particles. The climate impact of interactive dust will be inspected in a companion study, although the global averaged effect of dust upon climate is briefly discussed in section 6.

2. Model and Experiments

The soil dust aerosol model embedded in the GISS AGCM is described in detail in *Tegen and Miller* [1998]. In this model, the soil dust particles are partitioned in 4 size classes ($< 1\,\mu$m, $1-2\,\mu$m, $2-4\,\mu$m, $4-8\,\mu$m), which are carried as separate tracers. Particles smaller than $1\,\mu$m are transported as one class because they are not strongly fractionated by gravitational settling. Particles larger than $8\,\mu$m are responsible for only

about 1% of the dust radiative forcing [*Tegen et al.*, 1996]. The surface distributions of clay (particles smaller than 1 μm) and small silt (particle radius between 1 μm and 10 μm) were derived from a global soil texture data set [*Zobler*, 1986; *Webb et al.*, 1991].

The dust deflation is parameterized according to *Gillette* [1978]. It is proportional to the cube of the surface wind speed, with the constraint that the speed must exceeds a threshold velocity,

$$q_a = C(u - u_{tr})u^2, \tag{1}$$

where q_a is the dust flux from the surface in $\mu g\,m^{-2}\,s^{-1}$, u is the surface wind speed in $m\,s^{-1}$, and u_{tr} is the threshold velocity. C is a dimensional constant which amounts to $2\,\mu g\,s^{-2}\,m^{-5}$ and $5\,\mu g\,s^{-2}\,m^{-5}$ for clay, and silt, respectively. The threshold velocity varies between 4 and $10\,m\,s^{-1}$ depending on the location. The variations are designed to partly account for subgridscale wind variability [*Tegen and Miller*, 1998]. In addition, dust emission only can occur, when the soil moisture is low. To fulfill this condition in the model, the evaporation in a grid box must exceed precipitation for a certain time period which depends on the soil texture. In addition, dust deflation is only allowed in desert or sparsely vegetated areas labeled by *Matthews* [1983], as well as from disturbed soils which are affected by deforestation, cultivation in dry regions, wind erosion, and the shift in the Saharan/Sahelian boundary [*Middelton*, 1992; *World Resources Institute*, 1992; *Tucker et al.*, 1991].

Dust removal takes place by gravitational settling, turbulent mixing in the first

model layer, and subcloud wash-out which is calculated using AGCM precipitation. The efficiency of the dust removal by rain is described using the scavenging ratio Z,

$$Z = C_{rain}/C_{air}, \tag{2}$$

where C_{rain} is the dust concentration in rain in grams of dust per kilogram of rainwater and C_{air} is the aerosol concentration in air in units of grams of dust per kilogram of air. Here, a scavenging ratio of 700 is used according to *Tegen and Fung* [1994].

The updated version of the GISS AGCM [*Hansen et al.*, 1983], in which the soil dust model was implemented, has a horizontal resolution of $4° \times 5°$ and 12 vertical layers. The AGCM version used here has a new convection/cloud scheme and ground hydrology parameterization [*DelGenio et al.*, 1996; *Hansen et al.*, 1997]. Dust radiative effect was calculated with the GISS AGCM radiation model (k-distribution, doubling-adding). Radiative parameters for the different particle sizes were determined via Mie-calculations using refractive indices for far-traveled Saharan dust from *Volz* [1973] and *Patterson and Gillette* [1977]. For the calculation of dust radiative effect, the submicron size class was further subdivided into 4 size classes according to *Tegen and Lacis* [1996].

Four experiments were carried out using both a prescribed climatological sea surface temperature (SST) and sea ice distribution as a lower boundary condition. Preliminary studies with a mixed layer ocean as a lower boundary show that the climate response to dust over land is similar to integrations using fixed SSTs; therefore, we do

not expect significant changes to the results presented here were SST to be calculated. In one of the four experiments, dust was a dynamic tracer only without affecting the radiation. In the remaining three experiments, radiative forcing by dust was taken into consideration. The single scattering albedo of far-traveled Saharan dust particles (ϖ_0) was prescribed in the first of these three experiments. It depends on the dust size and the wavelength (1 μm size: $\varpi_0 = 0.86$; 0.5 μm size: $\varpi_0 = 0.92$ at 0.55 μm wavelength). Hereafter, we are referring to this experiment as the "baseline experiment". In the remaining two experiments, the single scattering albedo was decreased or increased by 10%, representing more absorbing ($0.9\varpi_0$) or reflecting dust ($1.1\varpi_0$), respectively, to evaluate the sensitivity of the dust cycle to changing radiative properties of the dust particles. For the more reflecting case, the dust single scattering albedo was capped at 1.0. The first year of model output was discarded to eliminate trends associated with spin-up, after which 26 years were simulated in each experiment.

3. Sensitivity of the Soil Dust Emission

3.1. Some Remarks About the Approach

Within a source region, dust emission is favored by high surface winds and evaporation exceeding precipitation over an extended period of time. Changes in the wind speed, that change the dust emission can occur over various space and times scales. These can be local phenomena which affect the variability in short time scales, or changes in the large-scale quasi-stationary patterns of the circulation.

To identify the processes that change dust emission in the main source regions, we calculated the local correlation coefficients between the monthly averaged dust source flux and other variables. These variables were the monthly averaged number of wind events above the threshold velocity for dust emission (n_{tr}), the monthly averaged wind speed (v), the magnitude of the monthly averaged horizontal wind vector ($\|\vec{v}\|$), and the monthly averaged difference of precipitation and evaporation (P – E). We expected the highest correlations between the dust source flux and n_{tr}. v includes fluctuations at short and long time scales, since it is calculated from the horizontal wind vector at each time step. By calculating the magnitude of the monthly averaged wind vector $\|\vec{v}\|$, changes in wind speed on a short time scale are averaged out. Hence, changes in $\|\vec{v}\|$ can be interpreted as changes in the circulation on a monthly or longer time scale. We expect less correlation between this variable and the dust source flux, compared to the correlation between the dust source flux and both n_{tr} and v. In this section, we discuss the cause of changes in the patterns of dust emission obtained in our experiments. We are interested in the seasonal mean of the changes in the variables. Thus, differences are shown for the seasonal average (December/January/February – DJF; March/April/May – MAM; June/July/August – JJA; September/October/November – SON; annual values – ANN). However, calculating a correlation between the seasonal averages of two variables can lead to misinterpretation, because anomalies in time from the seasonal average can be caused by anomalies in different months of a season. Those would lead to a faulty positive (or negative) correlation coefficient. Therefore, the correlations were calculated using the monthly averages of the variables to minimize such source of error.

The correlation between P − E and the dust source flux was also calculated because this difference is a constraint upon the dust source flux. However, we did not find any significant correlation between changes in P − E and changes in the dust source flux. Changes in this constraint have only a little effect on the dust source flux variability with respect to its sensitivity to the single scattering albedo of dust particles.

3.2. Global Dust Emission

In the AGCM experiment in which dust is a dynamic tracer with no radiative effect, the globally averaged dust emission is $1312 \pm 97\,\mathrm{Mt\,yr^{-1}}$ (mean plus or minus one standard deviation based on yearly means). This amount is about 40% larger than the emission obtained from a similar experiment carried out in a former study with the 9 layer GISS GCM [experiment A in *Tegen and Miller*, 1998]. The difference is caused by higher wind speeds at the surface using the 12 layer version of the model for the current study. Nevertheless, the value is within the range of other estimates which are widely separated [see *Duce*, 1995].

A comparison of the total dust emission in the various experiments is given in Table 1. The time mean and the interannual standard deviation are presented both for the entire year and the individual seasons. In the experiment with radiatively inactive dust, the reference experiment, the emission shows a maximum in Northern Hemisphere (NH) spring and summer, and a minimum in autumn. In the experiments including the radiative effect of dust, the yearly emitted amount of dust is about 15 to 20% lower than in the reference experiment. In the course of the year, the reduction varies both with

the season and the prescribed single scattering albedo. In winter, the largest decrease is found for more absorbing dust, whereas in summer, the largest decrease is found for more reflecting dust. There is also a tendency of decreased interannual variability in the experiments which include the radiative effect of dust.

3.3. Saharan/Sahelian Source Region

The largest contribution to globally emitted dust is from the Saharan/Sahelian source region (Table 2). This regions emits $592 \pm 55\,\mathrm{Mt\,yr^{-1}}$ of dust in the reference experiment. This value is reduced by 12 to 15% in all experiments which include the radiative effect of dust. However, this reduction occurs in different season depending on the particle single scattering albedo. During NH winter, dust emission is most reduced for more absorbing dust, whereas for summer, dust emission is most reduced for more reflecting dust.

Plate 1 displays the horizontal distribution of the seasonally averaged dust source flux (numbers) and surface wind vector (arrows) in the Saharan/Sahelian region in NH winter of the reference experiment, along with changes in the experiments with radiatively active dust. In addition, correlations (shades) between source flux and $||\vec{v}||$ are shown. For the reference experiment, the correlations were calculated between the absolute values of the variables using monthly values from this season. For the experiments with radiatively active dust, they were calculated between the responses with respect to the reference experiment. All correlation coefficients of colored grid boxes in this plate and the plates of the other source regions are statistically significant

(t-test) at a confidence level of 95% or greater.

During NH winter in the reference experiment, the Sahel region along with the western and eastern Sahara most contribute to the total dust emission in North Africa. The emission is positively correlated with $\|\vec{v}\|$ which is related to the trade winds in this region, in particular in western Sahara and the Sahel region.

For more absorbing dust, the strong decrease in dust emission relative to the reference experiment is mainly found in the eastern part of the Saharan/Sahelian source region, whereas there is actually an increase in the emission in northwestern Sahara. Some positive correlation between the change in the dust source flux and the change in the quasi-stationary circulation is found both in northwestern Africa and in the eastern Sahel. The visual examination of the difference vector of the seasonally averaged surface wind indicates an increase and decrease, respectively, in the trade winds in these both regions. In the other two experiments with radiatively active dust, the winter changes in the dust source flux are generally smaller. The grid boxes in western Africa where the source flux increases have only a minor contribution to the total source flux in North Africa.

During NH summer in the reference experiment (Plate 2), the largest contribution to the dust emission in North Africa originates from the northeastern and eastern part. In this region, the dust source flux is positively correlated with the large scale circulation, in particular with the Indian monsoon flow over eastern Africa.

In the experiments with radiatively active dust, dust emission in the Saharan/Sahelian source region is most reduced in the experiment with more reflecting dust

(see Table 2), because of a significant decrease in the emission in northeastern Africa. In several grid boxes, where an evident change in the dust source flux is found, those changes are positively correlated with changes in $\|\vec{v}\|$. The visual examination of the stationary wind vector reveals that these changes are linked to changes in the Indian monsoon circulation. For more absorbing dust, the monsoon induced flow is strongly enhanced, whereas for more reflecting dust, the Indian monsoon is weakened. In both cases, this leads to a specific pattern of changes in the dust emission. In the baseline experiment, a slightly strengthened monsoon is found. Especially for more reflecting dust, the decrease in the Indian monsoon causes the strong decrease in the emitted dust integrated over the whole region. However, the correlations between changes in the monthly averaged dust emission and changes in v, which were also calculated, are evidently higher and statistically significant in more grid boxes than the correlations between changes in the source flux and changes in $\|\vec{v}\|$, indicating that the changes in dust emission cannot only be explained by changes in the large-scale quasi-stationary circulation. Processes with short time scales also seem to have an important effect on the changes in the dust emission in North Africa.

3.4. Arabian Peninsula's Source Region

The dust emission from the Arabian peninsula has two peaks, one in winter and the other one in summer (Table 2). In the reference experiment, the total amount of the yearly emitted dust is $56.5 \pm 11.9\,\mathrm{Mt\,yr^{-1}}$. For more absorbing dust, this amount is about 10% higher, but for more reflecting dust about 20% lower, a difference that

can be attributed mainly to the NH summer months. In the other seasons, there is a tendency of a reduced dust emission for all experiments with radiatively active dust.

The largest part of the dust amount emitted from the Arabian peninsula in the reference experiment originates along the Yemeni coast (Plate 1 and Plate 2). An additional amount comes from a grid box at the head of the Persian gulf.

In the experiments with radiatively active dust, the main changes in the emission are found in NH summer (Plate 2). The emission increases both at the head of the Persian gulf and the Yemeni coast for more absorbing dust and, with a smaller magnitude, in the baseline experiment, whereas it decreases at these grid boxes given more reflecting dust. These changes are positively correlated with changes in $\|\vec{v}\|$. They are related to an enhanced (diminished) Indian monsoon circulation for more absorbing (reflecting) dust.

3.5. Central Asia's Source Region

Here, Central Asia is defined as the region around the Caspian sea and the Aral sea. Central Asia's dust emission in the reference experiment shows a strong annual cycle with a maximum of $107 \pm 40\,\mathrm{Mt\,3mo^{-1}}$ in NH summer and a minimum of only $5 \pm 3\,\mathrm{Mt\,3mo^{-1}}$ in winter (Table 2). The yearly emission amounts to $211 \pm 58\,\mathrm{Mt\,yr^{-1}}$, which is reduced in each experiment with radiatively active dust. This reduction increases with increasing single scattering albedo from $36\,\mathrm{Mt\,yr^{-1}}$ for $0.9\varpi_0$ to $72\,\mathrm{Mt\,yr^{-1}}$ for $1.1\varpi_0$, largely as a result of differences during the NH summer months.

Plate 3 displays the horizontal distribution of the dust emission in the reference

experiment during Northern Hemisphere summer, its changes in the experiments with radiatively active dust, and its correlation with the surface wind speed. In the reference experiment, the main areas of dust emission are located north of the Caspian sea and east of the Aral sea. North of the Caspian sea, dust emission is smaller in all experiments that include radiatively active dust. In contrast, the changes in the emission depend on the single scattering albedo in the Aral sea region. There, the emission increases for more absorbing dust, whereas they decrease for more reflecting dust. There is some positive correlation of these changes with changes in the surface wind speed, which increases (decreases) in this region, in particular southeast of the Aral sea, for more absorbing (reflecting) dust. In many grid boxes, there is also a strong correlation of the changes in the dust source flux with changes in the number of wind events above the critical threshold velocity. In contrast, there are only uncertain results from the correlation between dust emission and large-scale circulation. Generally, these results indicate that the described changes in the dust emission are mainly due to changes both in mean wind speed and wind speed variability on shorter time scales.

3.6. China's Source Region

China's dust source region emits $55.2 \pm 21.5\,\mathrm{Mt\,yr^{-1}}$ in the reference experiment (Table 2). The largest amount is contributed during NH spring. In this season, a maximum of $39.3 \pm 17.4\,\mathrm{Mt\,3mo^{-1}}$ is found. In contrast, only little dust is emitted during winter and autumn. The implementation of the radiatively active dust generally leads to a reduced dust emission. In all seasons, except in winter, dust emission decreases

with increasing particle absorptivity. The relative decrease in dust emission is largest in summer. The annual emission is reduced by 35% and 13% for $0.9\varpi_0$, and $1.1\varpi_0$, respectively.

The horizontal distribution of dust emission in China's source region and correlations are not shown because of a lack of significance of the correlation between the dust source flux and the other variables. In the reference experiment, the region which mainly contributes to the total dust emission is located between 105° and 120°E and 40° and 48°N. In particular during NH summer, when the relative reduction in the emission is largest, few grid boxes with a positive correlation between changes in the dust source flux and changes in the surface wind speed as well as in n_{tr} are found. We did not find any correlation with $\|\vec{v}\|$. This indicates that decreased dust emission in China's source region is mainly caused by processes with small time scales, and not due to changes in the large-scale circulation. This dependence is similar to that in Central Asia.

3.7. North America's Source Region

The dust emission in North America amounts to $114 \pm 42\,\mathrm{Mt\,yr^{-1}}$ in the reference experiment (Table 2). In NH spring, the maximum amount is emitted corresponding to $44 \pm 21\,\mathrm{Mt\,3mo^{-1}}$. The emission in each of the other seasons is about half of this value. In all seasons, less dust is emitted in the experiments that include the radiatively active dust. The reduction of the annual total is between 12% and 33%.

Plate 4 displays the horizontal distribution of dust emission in the reference

experiment during NH spring, its changes in the experiments with radiatively active dust, and its correlation with the surface wind speed. In the reference experiment, dust emission is largest over the Great Plains. In particular in the southern part, dust emission is positively correlated with the surface wind speed.

In the experiment with radiatively active dust, dust emission is reduced in the southern part. In this region, it increases with increasing particle absorptivity (as in China). These changes show some positive correlation with changes in the surface wind speed, in particular for more absorbing dust and in the baseline experiment. In addition, there is an even stronger correlation with the number of wind events. In the northern source region, there is also a tendency of reduced emission in all experiments with radiatively active dust, but with no clear dependence on the particle single scattering albedo. We did not find any correlation between changes in the dust emission and changes in $||\vec{v}||$. This indicates that the reduction in the dust emission is mainly due to processes with short time scales related to a decrease both in the wind speed and its variability.

3.8. Australia's Source Region

Australia's dust emission amounts to $225 \pm 54\,\mathrm{Mt\,yr^{-1}}$ in the reference experiment (Table 2). Almost half the amount is contributed during Southern Hemisphere (SH) summer. The minimum in the annual cycle is found during SH winter. In the experiments with radiatively active dust, the yearly averaged emission is about 20% lower in the yearly average. In the various seasons, the decrease ranges from 11 to

27% without any clear dependence on either the particle single scattering albedo or the season.

In Plate 5, the horizontal distribution of the dust source flux in the reference experiment, its changes in the experiments with radiatively active dust, and its correlation to the surface wind speed in Australia during SH summer are presented. In the reference experiment, dust is emitted over the whole central part of Australia with a maximum from a grid box located along the southern coast. The dust source flux is positively correlated with the surface wind speed where maximum emission is found.

A significant decrease in dust emission is found in all of the experiments that include the radiative effect of dust. The changes in the dust emission are positively correlated with changes in the surface wind speed. There is a more evident correlation of the change in the dust source flux with a change in the number of wind events above the critical threshold velocity. We did not find any correlation between the changes in the emission and changes in $\|\vec{v}\|$. Also in this region, changes in emission seem mainly be caused by changes in the mean wind speed and changes in the wind speed variability on a short time scale.

In this section, we have analyzed how the dust emission changes, if the radiative effect of dust is taken into consideration in the model. In summary, we have shown that this radiative effect leads to a reduced dust source flux into the atmosphere for the global average in all season and for almost all main dust source regions. In general, this indicates a negative feedback of dust radiative forcing upon dust emission. The amount of the reduction varies both with the season and with the single scattering albedo of

dust particles, depending on the region where dust deflation takes place. During winter in each hemisphere, in all regions with significant deflation, the reduction is larger for more absorbing than for more reflecting dust. During summer, this trend is generally reversed – the reduction in emission is larger for more reflecting dust, apart from China and North America.

In the Saharan/Sahelian source region, and in the Arabian peninsula, we found a positive correlation, which is statistically significant, between changes in the dust emission and changes in the magnitude of the monthly averaged surface wind vector which represents large-scale circulation patterns. In winter, changes in the dust source flux are related to changes in the trade winds, whereas in summer, they are related to changes in the Indian monsoon circulation.

4. Dust Concentration in the Experiments

The global mean and standard deviation of dust concentration in the various experiments are presented in Table 3; the atmospheric dust load has features which are similar to those of the dust emission. In the reference experiment, the annual and global mean dust concentration averaged over all layers amounts to $3.71 \pm 0.25\,\mu g\,kg^{-1}$. The dust load has its maximum in NH spring and summer, and its minimum in autumn. In the experiments that includes the radiative effect of dust, the yearly averaged dust concentration is reduced. The reduction ranges from 13 to 21%, varying according to season and prescribed single scattering albedo. In winter, the largest decrease is found for more absorbing dust, whereas in summer, the largest decrease is found for more

reflecting dust. There is also a tendency toward decreased variability in the experiments that include the radiative effect of dust.

The horizontal distribution of dust concentration in the reference experiment during NH winter and summer, and its changes in the experiments with radiatively active dust are presented in Figure 1 and Figure 2, respectively. The changes relative to the reference experiment were tested for statistical significance using Student's t-test. The changes at a confidence level of 95% or greater are shown by shaded areas in the pictures.

In the reference experiment in NH winter (Figure 1a), a dust cloud is located over North Africa extending over the tropical Atlantic. The maximum is located over the southern part of North Africa. Another major dust cloud is located over Australia, and a minor maximum of the dust concentration is found over North America.

The change in the dust concentration due to radiative effect of dust evidently varies over the various dust source regions depending on the season and the single scattering albedo. In winter, the dust concentration shows its strongest reduction of 20-30% over the Saharan/Sahelian source region in the experiment with more absorbing dust. In contrast, the dust concentration over this region is larger with increased single scattering albedo. This corresponds to enhanced dust emission in this region. Another source region which is perturbed by dust radiative forcing during NH winter is located in Australia. There, dust emission and concentration are reduced by 20-30% for radiatively active dust for all three values of the particle single scattering albedo of dust.

In summer (Figure 2), in contrast to winter, the strongest reduction of the

dust concentration is found in the experiment with more reflecting dust over the Saharan/Sahelian source region, and, additionally, over the Arabian peninsula and Central Asia which are also important source regions in this season. There, the dust load is about 50% lower in comparison to the reference experiment. In the experiment with more absorbing dust, this reduction is much smaller. Over the Arabian peninsula and north-eastern Africa, even an increase in the dust load is found. In contrast, the dust concentration decreases more strongly for more absorbing dust than for more reflecting dust over North America and China, although these are minor dust source regions in summer.

In NH spring and autumn, the changes in dust concentration as a result of dust radiative forcing show a transition state between the winter and summer change patterns. Despite the changes in the dust concentration, seasonal features like the spring maxima of the dust emission in North America and China are preserved in the experiments that include the radiative effect of dust.

In all seasons, the dust concentration is higher (lower) in high and mid-latitudes in low dust regions in the experiment with more absorbing (reflecting) dust. These changes are statistically significant because of a very small variability in the dust concentration in those regions. This response in the experiments with radiatively active dust could be caused by a longer (shorter) persistence of very small dust particles in the atmosphere due to a decreased (increased) deposition. Another possibility is an intensified (weakened) transport into the low dust regions.

We also compared the seasonal interannual variability by examining the standard

deviation of the dust concentration in the experiments. The experiments with radiative effect of dust do not differ significantly to another. However, there are some differences to the reference experiment.

In Figure 3, the standard deviation of the dust concentration during NH winter and summer, respectively, is presented for the reference and the baseline experiment. The interannual variability of the dust concentration is high, with a standard deviation 20 to 50% of the mean. In winter, the maximum values of the standard deviation are evidently smaller over the main dust source regions for radiatively active dust. The decrease amounts to about 30% and 50% over North Africa, and Australia, respectively. In the areas with low dust concentration, the interannual variability is similar for all experiments.

In contrast, the maximum NH summer values of the standard deviation do not significantly decrease in the baseline experiment. Over the Aral sea source region, even an evident increase which amounts to about 40% is found. A similar result was also obtained for more absorbing dust, whereas the interannual variability decreases in this region for more reflecting dust. In spring and autumn, the dust response resembles the results for winter. Changes in the seasonal interannual variability seem to reflect features of the changes in the seasonal long time averages. Where a decrease in the mean dust concentration is found there is also a tendency to a decreased variability and vice versa.

5. Comparison to AVHRR Satellite Data

5.1. Some Remarks About the Approach

To evaluate the model capability to reproduce the observed dust load in the atmosphere and its interannual variability, we compared the dust optical thicknesses from the experiments to satellite retrievals derived from the National Oceanic and Atmospheric Administration (NOAA) advanced very high resolution radiometer (AVHRR) instrument [*Rao et al.*, 1988; *Stowe et al.*, 1997; *Husar et al.*, 1997]. These data are available for the years 1982 to 1992 and 1996/97. Model dust extinction optical thicknesses are calculated according to *Tegen and Fung* [1994]. Such a comparison of modeled and satellite derived optical thickness is not straightforward. In the AVHRR satellite retrievals, dust is assumed to be totally reflecting. Thus, the retrievals provide a lower limit of the dust optical thickness in regions with high dust concentration, particular for more absorbing dust. For more reflecting dust, we can expect a closer agreement between modeled and measured optical thickness. In regions with low dust concentration, other aerosol types can significantly contribute to the optical thicknesses of the retrievals. There, the modeled optical thicknesses are expected to be lower than the satellite retrievals.

Another source of comparison uncertainty is the different size distributions of aerosol particles assumed by the AVHRR satellite retrievals [*Stowe et al.*, 1997] and the model. In the model, dust aerosol size distributions are calculated dynamically and vary with each grid box, whereas fixed sizes are assumed for satellite retrievals. An

additional complication is particle nonsphericity, which is not taken into consideration in the model. The comparison is also limited by the fact that the AVHRR retrievals only cover optical thicknesses over sea.

Despite these uncertainties, a comparison of the model results to the retrievals is a useful approach to identify regions where the model results are inconsistent with the observations, even if only a coarse evaluation is possible. As a consequence, we cannot distinguish which experiment best represents the observations.

5.2. Comparison of the Mean Optical Thickness

In Figure 4, the differences between the mean optical thickness from the baseline experiment and from the AVHRR satellite are presented for NH winter, spring, and summer. To focus on features related to high optical thickness, these differences are only shown where the optical thickness is larger than 0.2 in the observations or in the experiment. In NH autumn, the dust optical thickness in the experiments is lower than 0.2 over all sea points. For that reason, this season has not been included in the evaluation.

In NH winter, the simulated dust optical thickness offshore the western coast of North Africa between 20°N and 30°N is about 0.1 higher than in the observations. This difference increases with decreasing single scattering albedo of dust and vice versa. Other aerosols than soil dust do not significantly contribute to the total optical thickness in this region [*Tegen et al.*, 1997]. Therefore, the observed optical thickness should in this region be a lower limit considering dust absorption. Regarding that the

dust load in this region does not change much with the radiative effect of dust in our various experiments, the simulated optical thickness is consistent with the observations. In contrast, in NH spring, the optical thickness in this region is overestimated in the experiments compared to satellite data, although, for radiatively active dust, the results are closer to observations than for radiatively inactive dust.

In NH winter and spring, over the equatorial Atlantic, carbonaceous aerosols significantly contribute to the total optical thickness [*Liousse et al.*, 1996; *Penner et al.*, 1998] so that the observed optical thickness should be higher than the simulated one. Therefore, the results of our experiments are not inconsistent with the observations.

In NH spring, the lower optical thickness east of the Chinese coast in the experiments is consistent with the observations, because China's deserts are an evident dust source during this season. In addition, sulfate and carbonaceous aerosols significantly contribute to the observed optical thickness in this region [*Tegen et al.*, 1997; *Penner et al.*, 1998; *Tegen et al.*, 1999]. The Indian subcontinent and the eastern Mediterranean are located at the edge of the dust cloud. These regions are also influenced by industrial aerosols. Thus, the lower optical thicknesses simulated in these regions are consistent with the observed ones.

In NH summer, in the areas with maximum dust concentration over the Arabian sea and Central Asia (represented by one grid box at the Caspian sea), the simulated optical thickness in the baseline experiment is higher by more than 0.4 compared to the observations, indicating an overestimation in the model, or an underestimation in the satellite retrievals. In contrast, further away from the center of the dust cloud,

over both India and the eastern Atlantic around 10°N, the dust optical thickness in the experiments is lower by more than 0.2 compared to the observations. This difference is more (less) negative for more absorbing (reflecting) dust, in particular over India. Since this region is also influenced by sulfate and carbonaceous aerosols, the simulated optical thickness is not inconsistent with the observation.

The atmospheric dust load in the model is evidently overestimated offshore western Australia during SH summer.

5.3. Comparison of the Interannual Variability

To evaluate the model capability to reproduce the interannual variability of the dust load in the atmosphere, we also compared the standard deviation of the seasonally averaged values.

An example, which is representative for all seasons, is the ratio of the standard deviation in the baseline experiment to the satellite data, shown in Figure 5 for the NH summer season. In regions with high dust optical thickness like in the Arabian sea, the model tends to overestimate the standard deviation compared to the observations, especially if the mean optical thickness is also overestimated. In contrast, in regions with low optical thickness, the simulated variability is evidently lower than the observed one. In the latter case, this could be explained by the neglecting of other aerosol types, which have a strong influence in those regions where the dust aerosol optical thickness is low.

6. Globally Averaged Climate Response

For all seasons, the global mean of some climate variables in the reference experiment, and their changes in the experiments with radiatively active dust are presented in Table 4. Regional variations will be described in a future article.

In the baseline experiment, the perturbation of net radiation due to radiative forcing by dust is about $-0.4\,\mathrm{W\,m^{-2}}$ at TOA and $-1.7\,\mathrm{W\,m^{-2}}$ at surface. That is, the main effect of soil dust aerosols is to redistribute radiative heating from the surface to the atmospheric column. This well agrees with the results obtained by *Miller and Tegen* [1998]. Compared to those, however, the response is less negative at surface and corresponds to greater cooling at TOA. *Miller and Tegen* [1998] studied the climate response using a prescribed distribution of the dust concentration and the 9 layer version of the GISS AGCM coupled to a mixed layer ocean model. Thus, the difference in the response could represent differences in the model, especially in the treatment of the ocean, or it may represent a measure of the uncertainty of model estimates of dust radiative forcing.

Both at TOA and surface, a negative anomaly by solar radiation is counteracted by a smaller positive anomaly by thermal radiation. In the annual average in both spectral ranges, the effect at surface is about four times the effect at TOA. The difference between top and surface anomaly is largest during NH summer and smallest during winter. The perturbation of absorbed solar radiation has an evident annual cycle with a minimum of $0.9\,\mathrm{W\,m^{-2}}$ in autumn and a maximum of $2.0\,\mathrm{W\,m^{-2}}$ in summer. This

corresponds to different dust concentrations in the atmosphere in these two seasons (see Table 3).

Higher absorptivity of the dust particles additionally decreases the net radiative flux at surface, and increases the radiative gain at TOA compared to the baseline experiment. Higher reflectivity has a reversed effect. The globally averaged solar radiation at surface is very sensitive to the particle single scattering albedo, in particular during NH summer. This is related to a strong sensitivity of the absorbed solar radiation in the atmospheric column; the absorbed solar radiation due to the radiative dust effect is in the case of more absorbing dust 2.25 times the value of the baseline experiment, and 12 times the value of the experiment with more reflecting dust. The emitted thermal radiation at surface more decreases with increased absorptivity due to larger cooling at surface under the dust cloud. In contrast, the anomaly of backscattered solar radiation at TOA decreases with increased absorptivity (i.e. decreased reflectivity) of the dust particles.

Even during NH winter, when the dust concentration is most reduced for more absorbing dust compared to the other experiments with radiatively active dust (see Table 3), the anomaly of absorbed solar radiation is largest in this experiment. In addition, during NH summer, the negative anomaly of solar radiation at TOA is largest in the experiment for more reflecting dust, indicating a stronger backscattering effect, although the dust concentration is most reduced here. That is, the direct effect of the changed radiative forcing due to variations in the single scattering albedo of dust particles (maybe combined with an effect due to changes in total cloud cover) dominates

the effect of the changed optical thickness due to the sensitivity of the atmospheric dust concentration to the single scattering albedo of dust particles.

Other variables are also sensitive to the radiative properties of dust particles. The globally averaged sensible heat flux at surface, which is negative, significantly increases with higher absorptivity. The surface net heating shows a negative response to the radiative effect of dust. The decrease which is larger for more reflecting than for more absorbing dust indicates that the radiative effect of dust tries to cool the surface. However, the lower boundary condition was prescribed in our experiments so that the SST cannot adapt to the surface net heat flux. For this reason, the global averaged surface air temperature is not listed in Table 4.

Both precipitation and evaporation decrease in the experiments that include the radiative effect of dust, in particular for more absorbing dust. The total cloud cover shows a slight tendency of increase (decrease) for more absorbing (reflecting) dust, except in NH summer. In this season the cloud cover diminishes in all experiments that include the radiative effect of dust.

7. Summary and Conclusions

Four experiments with a soil dust model embedded in the NASA/GISS AGCM were carried out. In one of them, dust was a passive tracer whose radiative effect was omitted. In the others, dust radiative effect was allowed to influence the model climate. The size and wavelength dependent single scattering albedo of far-traveled Saharan dust was prescribed in one of those experiments. However, dust optical properties should

vary with the mineralogical content of the source region. To estimate the importance of this effect, without undertaking the computational burden of parameterizing each source region individually, we repeated the experiment with radiatively active dust, this time increasing or decreasing by 10% the single scattering albedo of the dust particles. According to *Sokolik and Toon* [1999], this is a reasonable range of variability. In this paper, results have been presented both for the dust emission and the dust concentration in the atmosphere. The total dust deposition which also represents a part of the soil dust cycle has not been presented here, because the resulting changes in this variable are consistent with the results for emission and concentration.

The implementation of the radiative effect of dust into the model generally led to reduced soil dust emission and concentration on a global scale compared to the experiment where dust is transported as dynamic, but radiatively inactive tracer. That is, there is a negative feedback in the climate system due to the radiative effect of dust which counteracts the emission of soil dust. The reduction varies with the radiative properties of dust. During NH winter, the strongest decrease is found for more absorbing dust, and during summer, the strongest decrease is found for more reflecting dust.

The detailed analysis of the emission in the various main dust source regions showed that the reduction varies both with the season and the radiative properties of dust particles. In NH winter, lowering (raising) the single scattering albedo by 10% led to a reduced (increased) dust emission in the Saharan/Sahelian source region, compared to the baseline experiment. In contrast, in NH summer, the reduction is smallest (largest) for more absorbing (reflecting) dust. In summer, a similar sensitivity was found for

Arabian peninsula's source region and the region around the Aral sea. In both regions, even an increase in the emission was found for more absorbing dust, compared to the experiment with radiatively inactive dust. In contrast, in all seasons, the dust emission in China's source region is more (less) reduced for more absorbing (reflecting) dust than in the baseline experiment. A similar dependence on the single scattering albedo was found for North America's source region, in particular for its southern part. For Australia's source region, in SH summer, there is not any clear dependence of the emission on the radiative effect of dust particles.

We studied the relation of the changes in the dust emission to the changes in the surface wind for each season using correlation coefficients calculated from monthly averaged values. For the Saharan/Sahelian source region, and the Arabian peninsula, we found an evidently positive correlation between dust emission and large scale circulation features represented by the magnitude of the monthly averaged surface wind vector. During NH winter in our experiments, the dust emission and its change with varying radiative properties of dust is related to the trade winds over the Saharan/Sahelian area. In summer, a relation to the Indian monsoon circulation was found in the eastern Sahara and the Arabian peninsula. The increase (decrease) in the dust emission from the Arabian peninsula for more absorbing (reflecting) dust is connected to an increased (decreased) monsoon circulation. In the case of other dust source regions, we did not find a relation of the emission to large-scale circulation patterns, but to the mean surface wind speed which is based on daily values. That indicates that processes with short time scales related to a high variability mainly determine the changes in the dust

source flux in most source regions.

The changes in the mean dust concentration in the atmosphere both due to the implementation of the radiative effect of dust and the variation in the radiative properties of dust are consistent with the results in the dust emission. For all seasons, we also compared the standard deviations of the seasonally averaged dust concentration in the various experiments to examine the interannual variability in the model. During all seasons, the variability decreases in the regions with maximum dust concentration in all experiments with radiatively active dust compared to the experiment with inactive dust, if the long-time mean of the concentration also decreases. In NH summer, the variability increases over the Arabian peninsula and Central Asia, if the radiative effect of dust is implemented, in particular for more absorbing dust and in the baseline experiment.

To evaluate the model capability to reproduce the average dust concentration and the interannual variability in all season, we compared the optical thickness simulated in the experiments to the observations from AVHRR satellite data. The simulated optical thickness well agrees with the observed one in NH winter over the North Atlantic, indicating a reliable dust concentration in the model in this region. Results which also are not inconsistent with the observations were obtained for the ocean regions east of China during NH spring and over India during spring and summer. In contrast, the model seems to overestimate the dust optical thickness over North Africa during spring, over the Arabian peninsula and Central Asia during summer, and over Australia during SH summer. However, since the satellite retrievals used for this comparison are based on

a single channel algorithm and therefore necessarily assume aerosol properties (some of which are more appropriate for sulfate than dust aerosols), this comparison is somewhat ambiguous.

The model tends to overestimate the interannual variability in regions with high dust optical thickness compared to satellite data, in particular if the mean optical thickness is also overestimated. In contrast, in regions with low optical thickness, the simulated variability is evidently lower than the observed one. The latter result might be related to an underestimated transport of fine particles by the model to regions far the sources, but is probably due to the fact that the satellite retrieval is determined by other aerosol types in those regions with low dust concentration.

In the baseline experiment, the dust aerosols had the radiative properties of far-traveled Saharan dust particles. However, the conclusion from our sensitivity experiments is that specifying the radiative properties appropriate for individual source regions might improve the simulated dust emission because of the different sensitivity of the soil dust emission to changing radiative features of dust. For this, variations in the mineralogical composition of dust need to be taken into account [*Sokolik and Toon*, 1999; *Claquin et al.*, 1999].

Corresponding to the sensitivity of the soil dust cycle, we also found a sensitivity of various climate variables, like TOA and surface radiation, temperature, precipitation, cloud cover and circulation to the radiative properties of dust particles. The sensitivity of the globally averaged climate variables we showed here is dominated by the direct effect due to the radiative properties of the dust particles (maybe combined with an

effect due to changes in total cloud cover), which generally overwhelms the effect of the changed optical thickness due to the sensitivity of the atmospheric dust concentration to the dust radiative forcing. The sensitivity of the climate response will be described in more detail in a companion paper. The effect on trade winds in North Africa and Indian monsoon circulation has already been a part of the analysis presented here.

The experiments described in this paper were carried out with a prescribed SST. The next step will be to repeat these experiments using the NASA/GISS AGCM coupled to a mixed layer ocean. In this way, we want to examine whether the results are robust, if the SST itself is calculated and the energy fluxes depending on it are included in the system of feedbacks. Since dust emission is generally a weak function of the large-scale circulation, which might be changed given calculated SST, we do not expect significant differences to the results from our experiments presented here. In addition, *Miller and Tegen* [1998] who compared the results of experiments using a mixed layer ocean to those using a fixed SST for a prescribed atmospheric dust concentration found only small differences in the land temperature response. The main difference in the responses was found for precipitation.

To assess the magnitude of the full feedback between dust cycle and climate response, it will be desirable to repeat such model experiments with the atmospheric GCM coupled to a dynamic ocean.

References

Alpert, P., Y. J. Kaufman, Y. Shay-El, D. Tanre, A. da Silva, S. Schubert, and J. H. Joseph, Quantification of dust-forced heating of the lower troposphere, *Nature*, *395*, 367–370, 1998.

Claquin, T., M. Schulz, Y. Balkanski, and O. Boucher, Uncertainties in assessing radiative forcing by mineral dust, *Tellus*, *50B*, 491–505, 1998.

Claquin, T., M. Schulz, and Y. J. Balkanski, Modeling the mineralogy of atmospheric dust sources, *J. Geophys. Res.*, *104*, 22,243–22256, 1999.

Coakley, J. A., and R. D. Cess, Response of the NCAR Community Climate Model to the radiative forcing by the naturally occurring tropospheric aerosol, *J. Atmos. Sci.*, *42*, 1677–1692, 1985.

DelGenio, A. D., M.-S. Yao, W. Kovari, and K. K.-W. Lo, A prognostic parameterization for global climate models, *J. Climate*, *9*, 270–304, 1996.

Dentener, F. J., G. R. Carmichael, Y. Zhang, J. Lelieveld, and P. J. Crutzen, Role of mineral aerosol as a reactive surface in the global troposphere, *J. Geophys. Res.*, *101*, 22,869–22,889, 1996.

Duce, R. A., Sources, distribution, and fluxes of mineral aerosol and their relationship to climate, in *Aerosol Forcing of Climate*, edited by R. J. Charlson, and J. Heintzenberg, vol. ES17 of *Dahlem Workshop Reports*, pp. 43–72, New York, John Wiley & Sons, 1995.

Genthon, C., Simulations of desert dust and sea salt aerosols in Antarctica with a general-circulation model of the atmosphere, *Tellus*, *44B*, 371–389, 1992.

Gillette, D., A wind tunnel simulation of the erosion of soil: Effect of soil texture, sandblasting, wind speed, and soil consolidation on dust production, *Atmos. Environ.*, *12*, 1735–1743, 1978.

Hansen, J., et al., Forcing and chaos in interannual to decadal climate change, *J. Geophys. Res.*, *102*, 25,679–25,720, 1997.

Hansen, J. E., G. L. Russell, D. Rind, P. Stone, A. Lacis, S. Lebedeff, R. Ruedy, and L. Travis, Efficient three-dimensional global models for climate studies: Model I and II, *Mon. Wea. Rev.*, *111*, 609–662, 1983.

Herman, J. R., P. K. Bhartia, O. Torres, C. Hsu, C. Seftor, and E. Celarier, Global distribution of UV-absorbing aerosols from Nimbus-7/TOMS data, *J. Geophys. Res.*, *102*, 16,911–16,922, 1997.

Husar, R. B., J. M. Prospero, and L. L. Stowe, Characterization of tropospheric aerosols over the oceans with the NOAA advanced very high resolution radiometer optical thickness operational product, *J. Geophys. Res.*, *102*, 16,889–16,909, 1997.

Joussaume, S., Three-dimensional simulations of the atmospheric cycle of desert dust particles using a general circulation model, *J. Geophys. Res.*, *95*, 1,909–1,941, 1990.

Li, X., H. Maring, D. Savoie, K. Voss, and J. M. Prospero, Dominance of mineral dust in aerosol light-scattering in the North Atlantic trade winds, *Nature*, *380*, 416–419, 1996.

Liao, H., and J. H. Seinfeld, Radiative forcing by mineral dust aerosols: sensitivity to key variables, *J. Geophys. Res.*, *103*, 31,637–31,645, 1998.

Liousse, C., J. E. Penner, C. Chuang, J. J. Walton, and H. Eddleman, A global three-dimensional model study of carbonaceous aerosols, *J. Geophys. Res.*, *101*, 19,411–19,432, 1996.

Marticorena, B., and G. Bergametti, Two-year simulations of seasonal and interannual changes of the Saharan dust emissions, *Geophys. Res. Lett.*, *23*, 1921–1924, 1996.

Matthews, E., Global vegetation and land use: New high-resolution databases for climate studies, *J. Clim. Appl. Meteorol.*, *22*, 474–487, 1983.

Middelton, N., *World Atlas of Desertification*, Edward Arnold, London, 1992.

Miller, R. L., and I. Tegen, Climate response to soil dust aerosols, *J. Climate*, *11*, 3247–3267, 1998.

Miller, R. L., and I. Tegen, Radiative forcing of a tropical direct circulation by soil dust aerosols, *J. Atmos. Sci.*, *56*, 2403–2433, 1999.

Moulin, C., C. E. Lambert, F. Dulac, and U. Dayan, Control of atmospheric export of dust from North Africa by the North Atlantic Oscillation, *Nature*, *387*, 691–693, 1997.

Patterson, E. M., and D. A. Gillette, Commonalities in measured size distributions for aerosols having a soil-derived component, *J. Geophys. Res.*, *82*, 2,074–2,082, 1977.

Penner, J. E., C. C. Chuang, and K. Grant, Climate forcing by carbonaceous and sulfate aerosols, *Clim. Dyn.*, *14*, 839–851, 1998.

Prospero, J., The atmospheric transport of particles to the ocean, in *Particle Flux in the Ocean*, edited by V. I. et al., pp. 19–26, John Wiley & Sons, 1996.

Rao, C. R. N., L. L. Stowe, E. P. McClain, J. Sapper, and M. P. McCormick, Development and application of aerosol remote sensing with AVHRR data from the NOAA satellites, in *Aerosol and Climate*, edited by P. V. Hobbs, and A. Deepak, Hampton, Va, 1988.

Schulz, M., Y. J. Balkanski, W. Guelle, and F. Dulac, Role of aerosol size distribution and source location in a three-dimensional simulation of a Saharan dust episode tested against satellite-derived optickal thickness, *J. Geophys. Res.*, *103*, 10,579–10,592, 1998.

Shine, K. P., and P. M. de F. Forster, The effect of human activity on radiative forcing of climate change: a review of recent developments, *Glob. Plan. Change*, *20*, 205–225, 1999.

Sokolik, I. N., and O. B. Toon, Incorporation of mineralogical composition into models of the radiative properties of mineral aerosol from UV to IR wavelengths, *J. Geophys. Res.*, *104*, 9,432–9,444, 1999.

Stowe, L. L., A. M. Ignatov, and R. Singh, Development, validation, and potential enhancements to the second-generation operational aerosol product at the National Environmental Satellite, Data, and Information Service of the National Oceanic and Atmospheric Administration, *J. Geophys. Res.*, *102*, 16,923–16,934, 1997.

Tabazadeh, A., M. Z. Jacobson, H. B. Singh, O. B. Toon, J. S. Lin, R. B. Chatfield, A. N. Thakur, R. W. Talbot, and J. E. Dibb, Nitric acid scavenging by mineral and biomass burning aerosol, *Geophys. Res. Lett.*, *25*, 4185–4188, 1998.

Tegen, I., and I. Fung, Modeling of mineral dust in the atmosphere: Sources, transport, and optical thickness, *J. Geophys. Res.*, *99*, 22,897–22,914, 1994.

Tegen, I., and I. Fung, Contribution to the atmospheric mineral aerosol load from land surface modification, *J. Geophys. Res.*, *100*, 18,707–18,726, 1995.

Tegen, I., and A. A. Lacis, Modeling of particle influence on the radiative properties of mineral dust aerosol, *J. Geophys. Res.*, *101*, 19,237–19,244, 1996.

Tegen, I., and R. Miller, A general circulation model study on the interannual variability of soil dust aerosol, *J. Geophys. Res.*, *103*, 25,975–25,995, 1998.

Tegen, I., A. A. Lacis, and I. Fung, The influence on climate forcing of mineral aerosols from disturbed soils, *Nature*, *380*, 419–422, 1996.

Tegen, I., P. Hollrigl, M. Chin, I. Fung, D. Jacob, and J. Penner, Contribution of different aerosol species to the global aerosol extinction optical thickness, *J. Geophys. Res.*, *102*, 23,895–23,915, 1997.

Tegen, I., D. Koch, A. A. Lacis, and M. Sato, Towards a global aerosol climatology: Preliminary trends in tropospheric aerosol amounts and corresponding impact on radiative forcing between 1950 and 1990, *J. Geophys. Res.*, 1999, submitted.

Tucker, C. J., H. E. Dregne, and W. W. Newcomb, Expansion and contraction of the Sahara desert from 1980 to 1990, *Science*, *253*, 299–301, 1991.

Volz, F. E., Infrared optical constants of ammonium sulfate, Sahara dust, volcanic pumice, and flyash, *Appl. Optics*, *12*, 564–568, 1973.

Webb, R., C. Rosenzweig, and E. R. Levine, A global data set of particle size properties, Tech. Rep. TM-4286, NASA, 1991, 33 pp.

Wefers, M., and R. Jaenicke, Global 3D distribution of desert aerosol from a numerical simulation, in *Proceedings 3rd International Aerosol Conference, Kyoto, Japan*, edited by S. Masuda, and K. Takakashi, pp. 1086–1089, 1990.

World Resources Institute, *World Resources 1992-1993*, edited by A. L. Hammond. Oxford Univ. Press, New York, 1992.

Zobler, L., A world soil file for global climate modeling, Tech. Rep. TM-87802, NASA, 1986, 32 pp.

R. L. Miller, NASA Goddard Institute for Space Studies, 2880 Broadway, New York, NY 10025. (e-mail: rmiller@giss.nasa.gov)

J. Perlwitz, Department of Applied Physics and Applied Mathematics, Columbia University in The City of New York, c/o NASA/GISS, 2880 Broadway, New York, NY 10025. (e-mail: jperlwitz@giss.nasa.gov)

I. Tegen, Max Planck Institute for Biogeochemistry, Tatzendpromenade 1a, D-07745 Jena, Germany. (e-mail: itegen@bgc-jena.mpg.de)

Received _____

[1]Also at NASA Goddard Institute for Space Studies, New York, New York

To appear in the special issue on Mineral Dust in the Journal of Geophysical Research – Atmosphere 2000

Table 1. Global mean and standard deviation (STDV) of emitted dust in [Mt $3mo^{-1}$] and [Mt yr^{-1}], respectively, in the experiment with radiatively inactive dust (R: reference), and in the experiments with radiatively active dust for more absorbing ($0.9\varpi_0$), baseline (ϖ_0), and more reflecting dust ($1.1\varpi_0$).

	R		$0.9\varpi_0$		ϖ_0		$1.1\varpi_0$	
Season	Mean	STDV	Mean	STDV	Mean	STDV	Mean	STDV
DJF	341	52	271	43	300	42	299	34
MAM	385	46	300	34	318	49	320	43
JJA	358	62	341	40	320	56	278	37
SON	228	43	170	25	182	36	176	29
ANN	1312	97	1081	71	1120	88	1073	68

Table 2. Mean and standard deviation (STDV) of dust emission in [Mt 3mo^{-1}] and [Mt yr^{-1}], respectively, from source regions in the experiment with radiatively inactive dust (R: reference), and in the experiments with radiatively active dust for more absorbing ($0.9\varpi_0$), baseline (ϖ_0), and more reflecting dust ($1.1\varpi_0$).

	Sahara/Sahel's Dust Emission							
	R		$0.9\varpi_0$		ϖ_0		$1.1\varpi_0$	
Season	Mean	STDV	Mean	STDV	Mean	STDV	Mean	STDV
DJF	186	35	145	37	164	30	176	29
MAM	196	37	158	24	166	32	169	31
JJA	152	38	155	31	138	30	125	23
SON	58	15	44	15	47	15	48	14
ANN	592	55	501	53	517	54	519	42
	Arabian Peninsula's Dust Emission							
	R		$0.9\varpi_0$		ϖ_0		$1.1\varpi_0$	
Season	Mean	STDV	Mean	STDV	Mean	STDV	Mean	STDV
DJF	20.0	7.0	17.9	7.0	19.3	6.4	19.5	6.1
MAM	9.1	5.7	6.4	3.2	6.6	2.7	6.3	3.1
JJA	21.3	8.7	32.1	15.9	22.2	8.2	13.1	4.6
SON	6.3	3.5	6.1	3.1	5.1	2.4	6.7	4.0
ANN	56.5	11.9	62.4	17.4	53.2	11.8	45.7	9.4

Table 2. (continued)

	Central Asia's Dust Emission							
	R		$0.9\varpi_0$		ϖ_0		$1.1\varpi_0$	
Season	Mean	STDV	Mean	STDV	Mean	STDV	Mean	STDV
DJF	5	3	4	3	6	5	6	5
MAM	62	31	48	24	47	26	43	18
JJA	107	40	100	37	93	55	69	22
SON	37	25	24	23	25	19	22	12
ANN	211	58	175	56	169	63	139	25
	China's Dust Emission							
	R		$0.9\varpi_0$		ϖ_0		$1.1\varpi_0$	
Season	Mean	STDV	Mean	STDV	Mean	STDV	Mean	STDV
DJF	1.8	1.7	1.4	1.3	2.1	2.6	1.4	1.4
MAM	39.3	17.4	28.9	11.9	30.2	12.0	34.5	13.8
JJA	11.4	6.3	4.2	4.5	7.7	5.1	9.2	5.1
SON	3.0	2.9	1.6	2.4	2.9	2.5	3.1	2.9
ANN	55.2	21.5	35.9	12.3	42.6	13.5	47.8	14.4

Table 2. (continued)

	North America's Dust Emission							
	R		$0.9\varpi_0$		ϖ_0		$1.1\varpi_0$	
Season	Mean	STDV	Mean	STDV	Mean	STDV	Mean	STDV
DJF	24	11	17	7	20	9	15	6
MAM	44	21	31	14	38	16	35	16
JJA	22	13	13	9	17	9	18	9
SON	25	15	15	9	26	14	18	8
ANN	114	42	76	21	100	25	86	25
	Australia's Dust Emission							
	R		$0.9\varpi_0$		ϖ_0		$1.1\varpi_0$	
Season	Mean	STDV	Mean	STDV	Mean	STDV	Mean	STDV
DJF	100	34	82	18	83	21	77	17
MAM	27	13	21	6	23	8	24	8
JJA	22	8	16	6	18	9	19	9
SON	75	27	59	17	55	20	55	19
ANN	225	54	179	28	180	36	175	25

Table 3. Global mean and standard deviation (STDV) of dust concentration [μg kg^{-1}(Air)] averaged over all layers in the experiment with radiatively inactive dust (R: reference), and in the experiments with radiatively active dust for more absorbing ($0.9\varpi_0$), baseline (ϖ_0), and more reflecting dust ($1.1\varpi_0$).

	R		$0.9\varpi_0$		ϖ_0		$1.1\varpi_0$	
Season	Mean	STDV	Mean	STDV	Mean	STDV	Mean	STDV
DJF	3.46	0.51	2.83	0.42	2.99	0.36	3.00	0.36
MAM	4.54	0.54	3.65	0.35	3.79	0.54	3.70	0.50
JJA	4.32	0.68	4.21	0.56	3.81	0.67	3.29	0.38
SON	2.53	0.47	2.28	0.27	2.02	0.27	1.81	0.27
ANN	3.71	0.25	3.24	0.22	3.15	0.26	2.95	0.19

Table 4. Global mean of various climate variables in the reference experiment (R), and their perturbations in the experiments with radiatively active dust for more absorbing ($0.9\varpi_0$), baseline (ϖ_0), and more reflecting dust ($1.1\varpi_0$).

Season	R	$0.9\varpi_0$	ϖ_0	$1.1\varpi_0$
TOA Net Radiation [$W\,m^{-2}$]				
DJF	9.0 ± 0.4	-0.2	-0.5	-0.7
MAM	0.5 ± 0.4	0.2	-0.3	-0.8
JJA	-8.6 ± 0.4	-0.3	-0.5	-0.5
SON	3.4 ± 0.3	-0.2	-0.4	-0.5
ANN	1.1 ± 0.2	-0.1	-0.4	-0.6
TOA Solar Radiation [$W\,m^{-2}$]				
DJF	238.3 ± 0.4	-0.3	-0.6	-0.8
MAM	230.6 ± 0.4	0.3	-0.3	-0.8
JJA	224.4 ± 0.3	-0.0	-0.5	-0.7
SON	234.7 ± 0.4	-0.4	-0.6	-0.7
ANN	232.0 ± 0.1	-0.1	-0.5	-0.7
TOA Thermal Radiation [$W\,m^{-2}$]				
DJF	-229.3 ± 0.2	0.1	0.1	0.1
MAM	-230.1 ± 0.2	-0.0	0.1	$+0.0$
JJA	-233.0 ± 0.2	-0.3	$+0.0$	0.2
SON	-231.3 ± 0.2	0.2	0.2	0.2
ANN	-231.0 ± 0.1	-0.0	0.1	0.1

Table 4. (continued)

Season	R	$0.9\varpi_0$	ϖ_0	$1.1\varpi_0$
Surface Net Radiation [$W\,m^{-2}$]				
DJF	119.6 ± 0.2	-2.3	-1.7	-1.0
MAM	112.2 ± 0.2	-2.6	-1.9	-1.3
JJA	107.5 ± 0.2	-3.3	-2.0	-1.0
SON	116.6 ± 0.2	-1.9	-1.1	-0.7
ANN	114.0 ± 0.1	-2.5	-1.7	-1.0
Surface Solar Radiation [$W\,m^{-2}$]				
DJF	170.7 ± 0.4	-3.2	-2.0	-1.0
MAM	164.3 ± 0.4	-3.8	-2.2	-1.1
JJA	158.3 ± 0.4	-5.0	-2.5	-1.0
SON	168.0 ± 0.4	-2.9	-1.5	-0.8
ANN	165.3 ± 0.2	-3.7	-2.1	-1.0
Surface Thermal Radiation [$W\,m^{-2}$]				
DJF	-51.1 ± 0.3	0.9	0.3	$+0.0$
MAM	-52.1 ± 0.3	1.2	0.4	-0.2
JJA	-50.9 ± 0.2	1.7	0.5	-0.1
SON	-51.5 ± 0.2	1.0	0.4	0.1
ANN	-51.4 ± 0.1	1.2	0.4	-0.0

Table 4. (continued)

Season	R	$0.9\varpi_0$	ϖ_0	$1.1\varpi_0$
Surface Sensible Heat Flux [$W\,m^{-2}$]				
DJF	-23.0 ± 0.2	1.1	0.7	0.2
MAM	-26.0 ± 0.2	1.6	0.8	0.1
JJA	-27.1 ± 0.2	1.9	0.9	0.1
SON	-23.7 ± 0.2	0.9	0.4	0.1
ANN	-25.0 ± 0.1	1.4	0.7	0.2
Surface Net Heating [$W\,m^{-2}$]				
DJF	8.2 ± 0.5	-0.2	-0.4	-0.6
MAM	-2.1 ± 0.4	-0.1	-0.5	-0.7
JJA	-9.5 ± 0.4	-0.2	-0.4	-0.6
SON	4.8 ± 0.5	0.2	-0.3	-0.5
ANN	0.4 ± 0.2	-0.1	-0.4	-0.6
Precipitation [$mm\,day^{-1}$]				
DJF	3.01 ± 0.02	-0.03	-0.02	-0.00
MAM	3.00 ± 0.02	-0.04	-0.02	-0.01
JJA	3.07 ± 0.01	-0.04	-0.02	-0.01
SON	3.03 ± 0.01	-0.04	-0.01	-0.00
ANN	3.03 ± 0.01	-0.04	-0.02	-0.01

Table 4. (continued)

Season	R	$0.9\varpi_0$	ϖ_0	$1.1\varpi_0$
Evaporation [mm day^{-1}]				
DJF	3.02 ± 0.02	-0.03	-0.02	-0.00
MAM	3.01 ± 0.02	-0.03	-0.02	-0.01
JJA	3.07 ± 0.02	-0.04	-0.02	-0.01
SON	3.00 ± 0.01	-0.04	-0.01	-0.00
ANN	3.03 ± 0.01	-0.04	-0.02	-0.01
Total Cloud Cover [%]				
DJF	51.4 ± 0.2	0.2	-0.1	-0.1
MAM	50.2 ± 0.2	0.1	-0.1	-0.3
JJA	51.4 ± 0.2	-0.2	-0.0	-0.1
SON	51.1 ± 0.2	0.4	0.2	$+0.0$
ANN	51.0 ± 0.1	0.2	-0.0	-0.1

Figure captions

Figure 1. Dust concentration [$\mu g\,kg^{-1}$] averaged over all layers in NH winter. a) reference experiment; difference to reference experiment for b) more absorbing dust, c) baseline experiment, and d) more reflecting dust. The light (dark) shades in b), c), and d) indicate statistically significant decreases (increases) at a confidence level of 95% or greater.

Figure 2. The same as in Figure 1, but in NH summer.

Figure 3. Seasonal standard deviation of the dust concentration [$\mu g\,kg^{-1}$]. a) reference experiment, and b) baseline experiment in NH winter; c), and d) same as a) and b), but in summer.

Figure 4. Difference between dust optical thickness (τ) in the baseline experiment and AVHRR satellite data for a) NH winter, b) spring, and c) summer.

Figure 5. Ratio of the standard deviation of the optical thickness simulated in the baseline experiment (SDTV(τ_{Sa})) to the standard deviation of the optical thickness derived from AVHRR satellite data (SDTV(τ_{Av})) in NH summer.

Plate captions

Plate 1. Dust source flux (numbers) [$\mathrm{mg\,m^{-2}\,d^{-1}}$], surface wind vector (arrows) [$\mathrm{m\,s^{-1}}$], and correlation (shades) between dust source flux and magnitude of the monthly averaged surface wind vector in the Saharan/Sahelian source region and in Arabian peninsula's source region, respectively, in NH winter. a) reference experiment; difference to reference experiment for b) more absorbing dust, c) baseline experiment, and d) more reflecting dust.

Plate 2. The same as Plate. 1, but in NH summer.

Plate 3. Dust source flux (numbers) [$\mathrm{mg\,m^{-2}\,d^{-1}}$], and correlation (shades) between dust source flux and surface wind speed in Central Asia's source region in NH summer. a) reference experiment; difference to reference experiment for b) more absorbing dust, c) baseline experiment, and d) more reflecting dust.

Plate 4. Dust source flux (numbers) [$\mathrm{mg\,m^{-2}\,d^{-1}}$], and correlation (shades) between dust source flux and surface wind speed in North America's source region in NH spring. a) reference experiment; difference to reference experiment for b) more absorbing dust, c) baseline experiment, and d) more reflecting dust.

Plate 5. Dust source flux (numbers) [$\mathrm{mg\,m^{-2}\,d^{-1}}$], and correlation (shades) between dust source flux and surface wind speed in Australia's source region in SH summer. a) reference experiment; difference to reference experiment for b) more absorbing dust, c) baseline, and d) more reflecting dust.

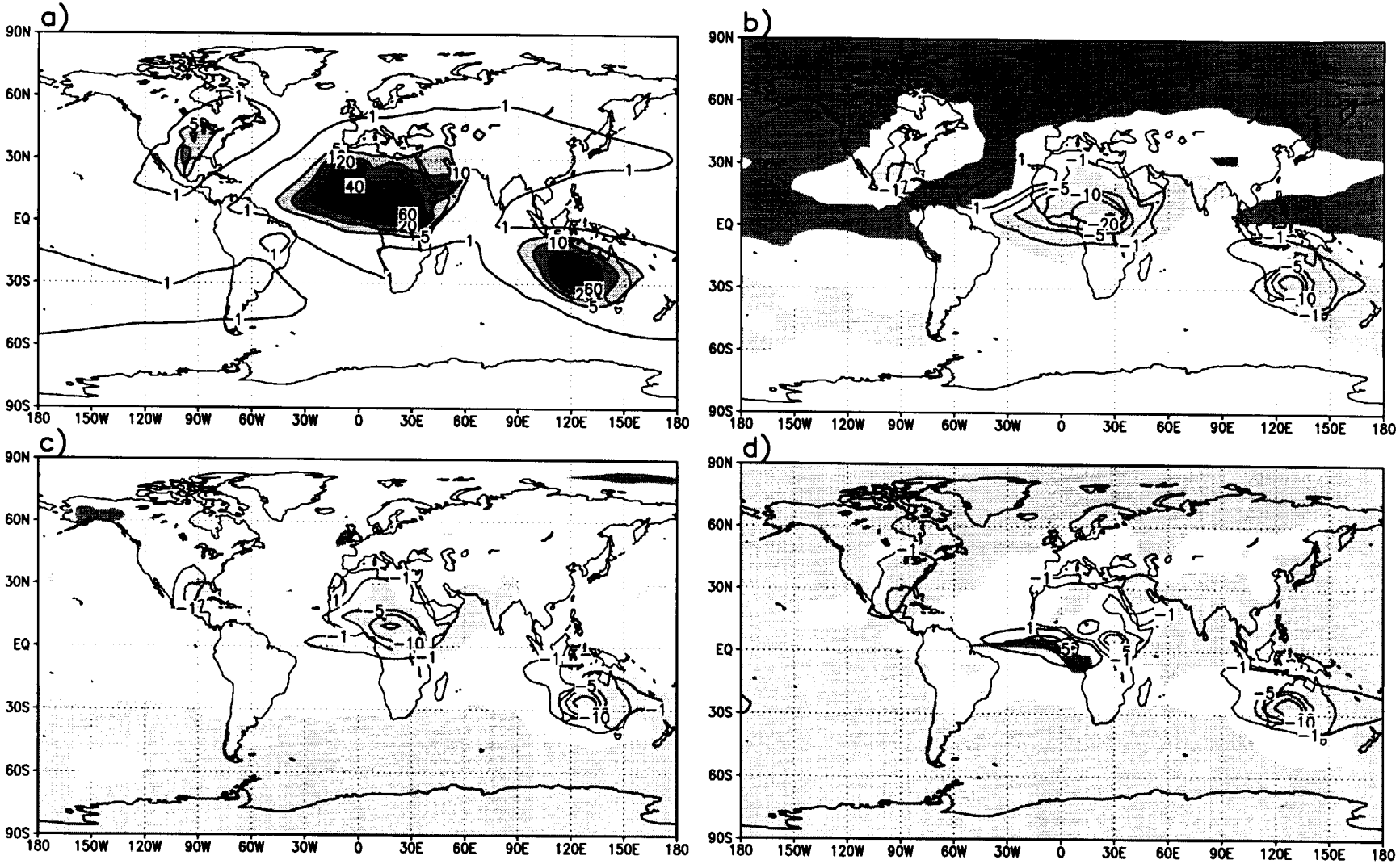
a)
b)
c)
d)
90N
60N
30N
EQ
30S
60S
90S
180 150W 120W 90W 60W 30W 0 30E 60E 90E 120E 150E 180

Figure 1

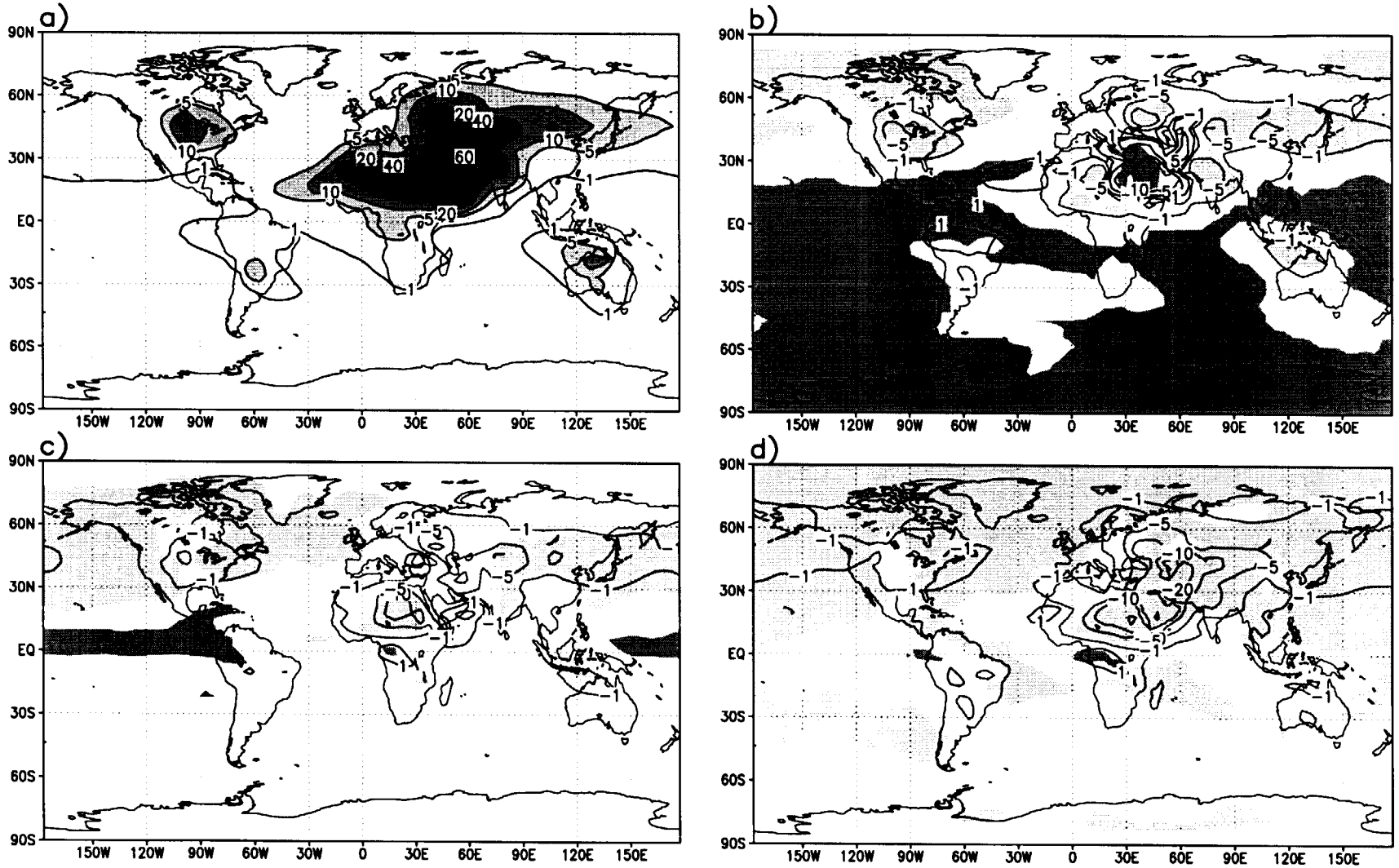
a)
b)
c)
d)
90N
60N
30N
EQ
30S
60S
90S
150W 120W 90W 60W 30W 0 30E 60E 90E 120E 150E

Figure 2

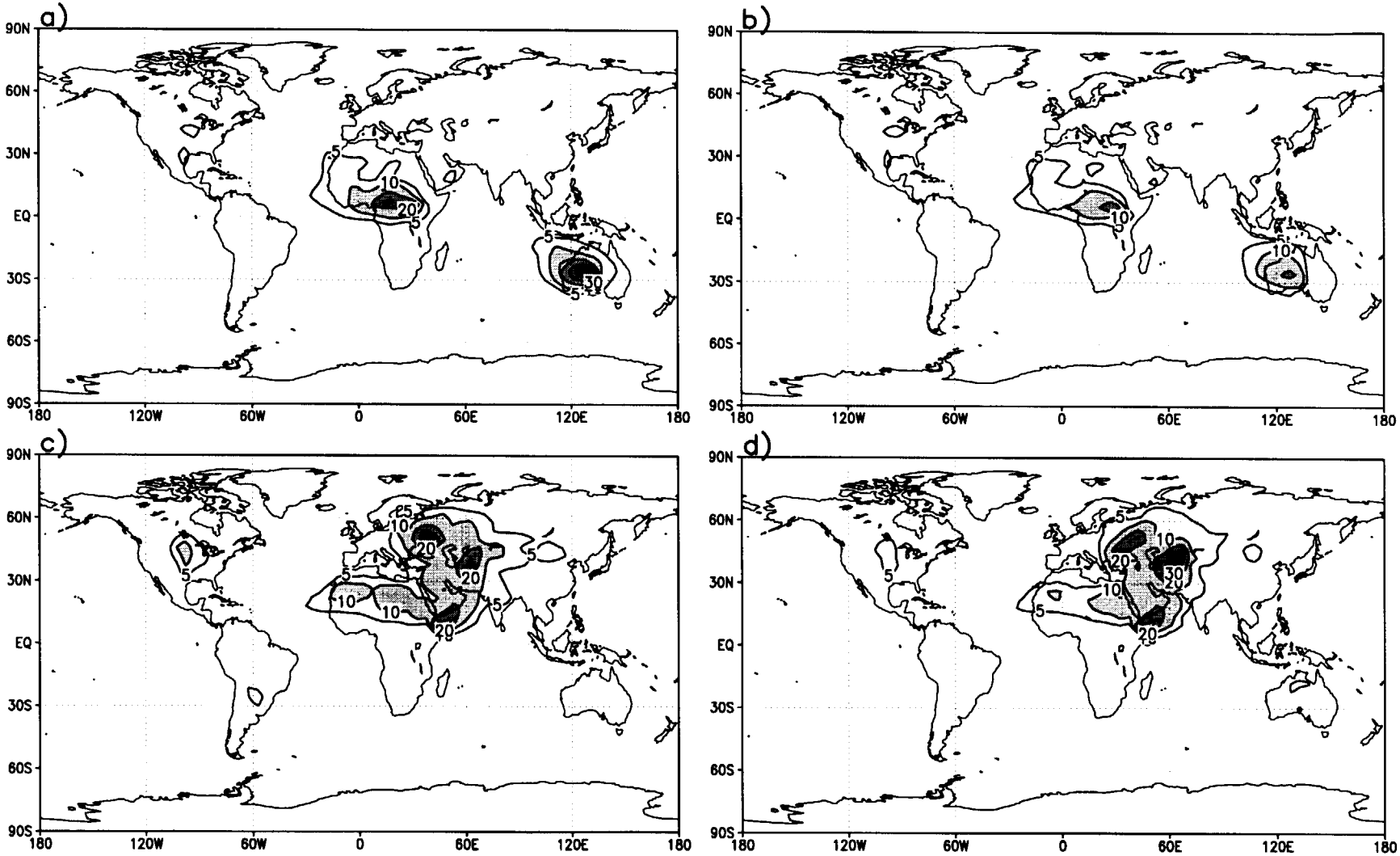

Figure 3

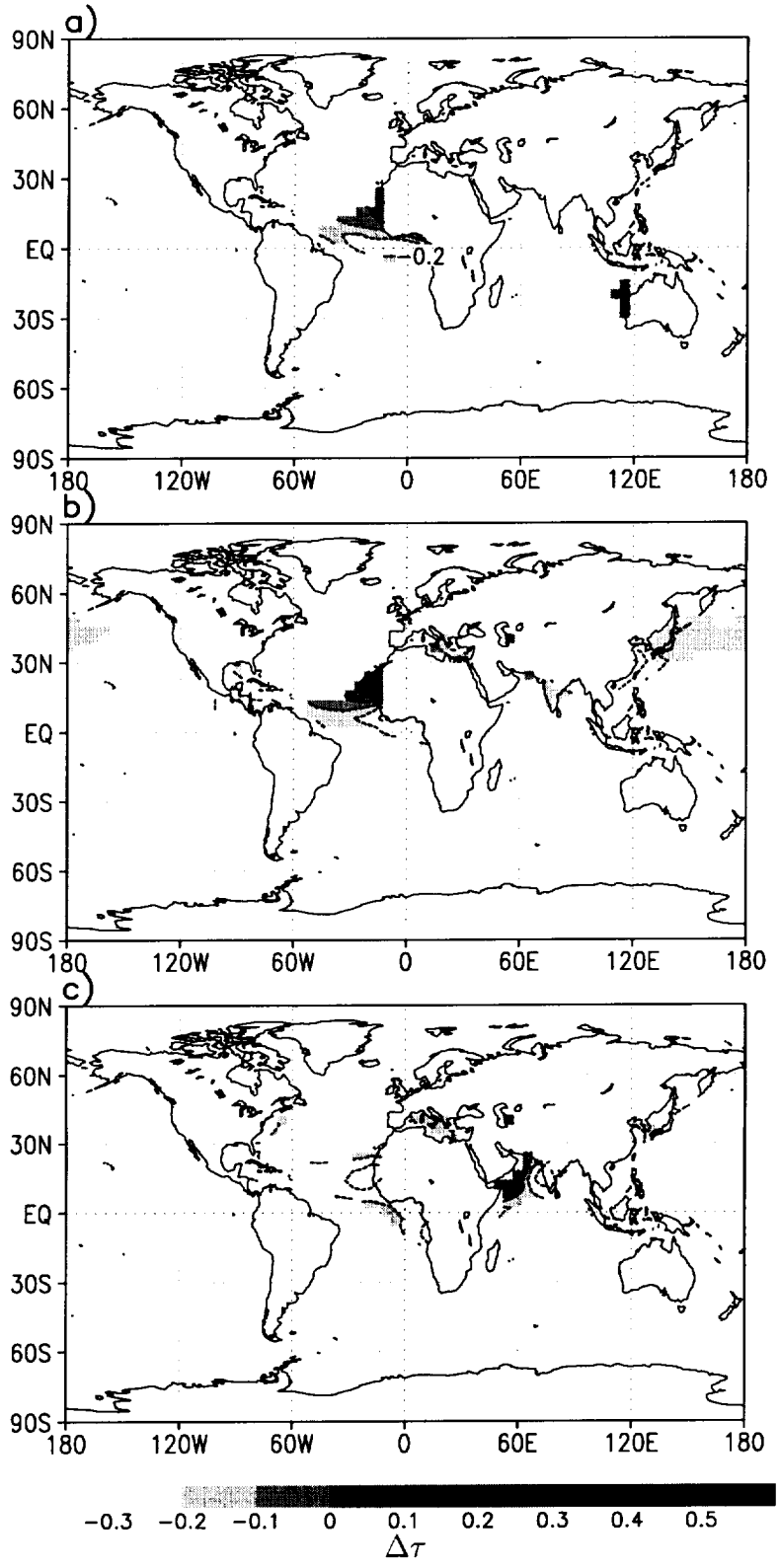
a)
b)
c)
90N
60N
30N
EQ
30S
60S
90S
180
120W
60W
0
60E
120E
180
−0.2
−0.3 −0.2 −0.1 0 0.1 0.2 0.3 0.4 0.5
Δτ

Figure 4

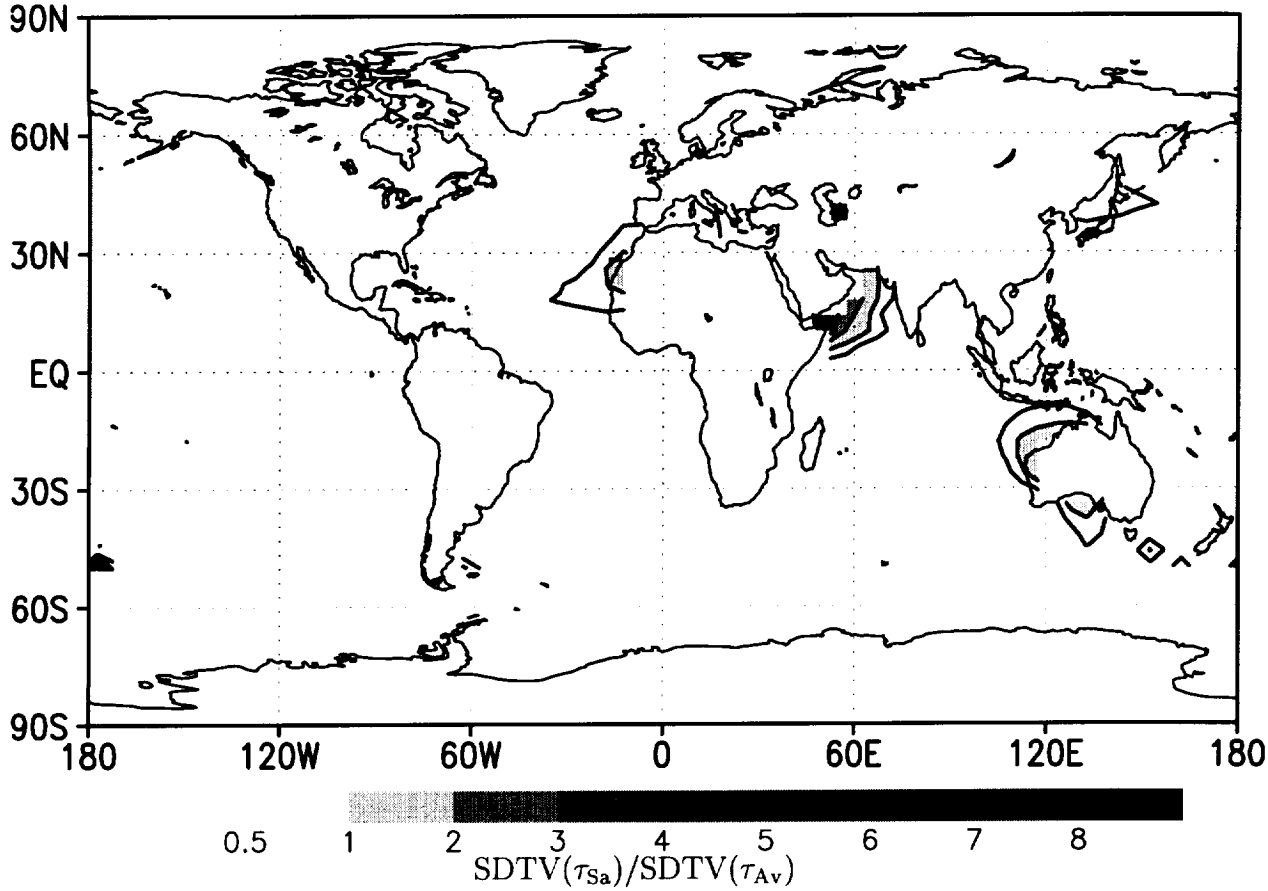
90N
60N
30N
EQ
30S
60S
90S
180
120W
60W
0
60E
120E
180
0.5
1
2
3
4
5
6
7
8
SDTV(τ_{Sa})/SDTV(τ_{Av})

Figure 5

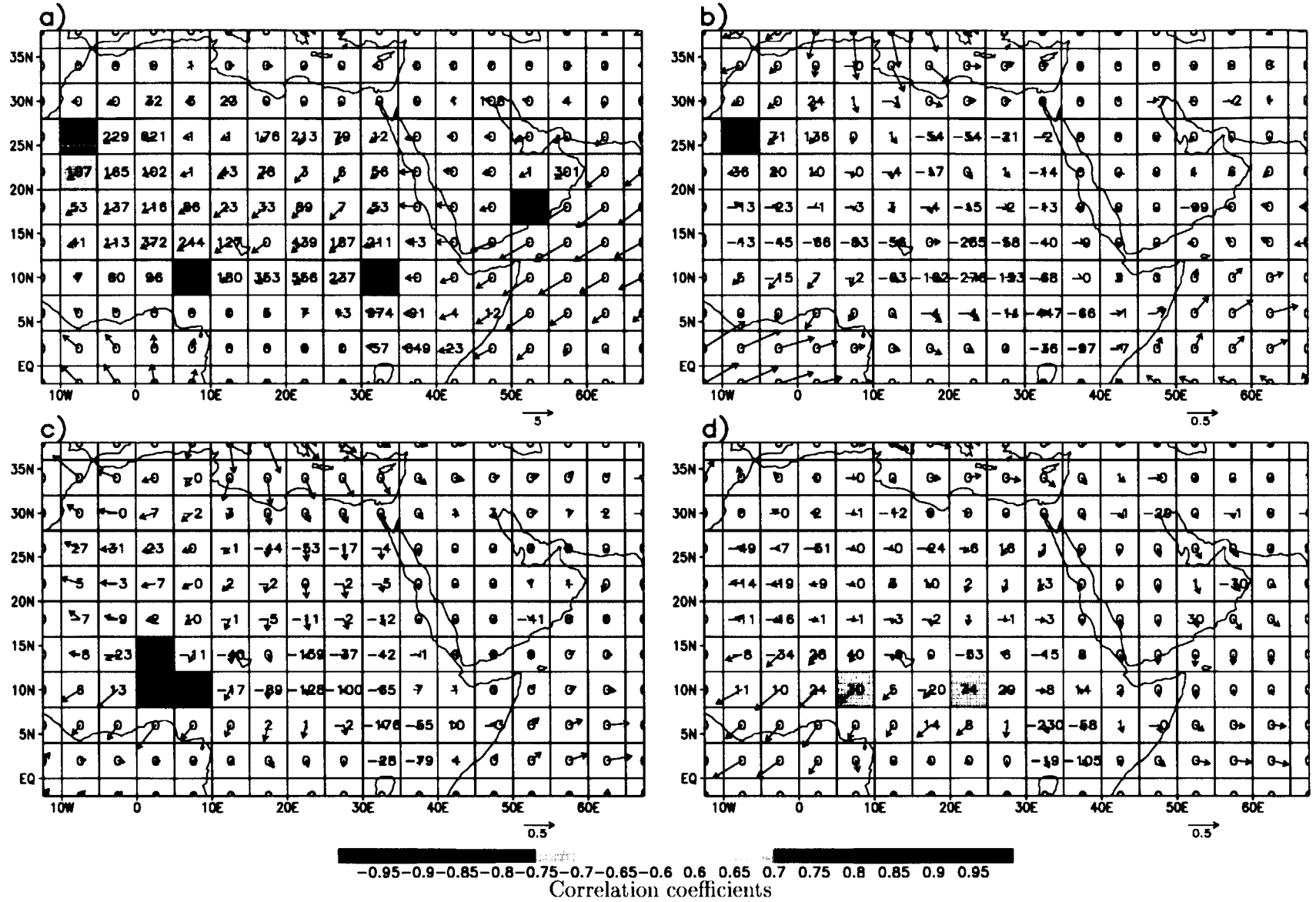
a)
b)
c)
d)
35N
30N
25N
20N
15N
10N
5N
EQ
10W
0
10E
20E
30E
40E
50E
60E
5
0.5
0.5
0.5
−0.95 −0.9 −0.85 −0.8 −0.75 −0.7 −0.65 −0.6 0.6 0.65 0.7 0.75 0.8 0.85 0.9 0.95
Correlation coefficients

Plate 1

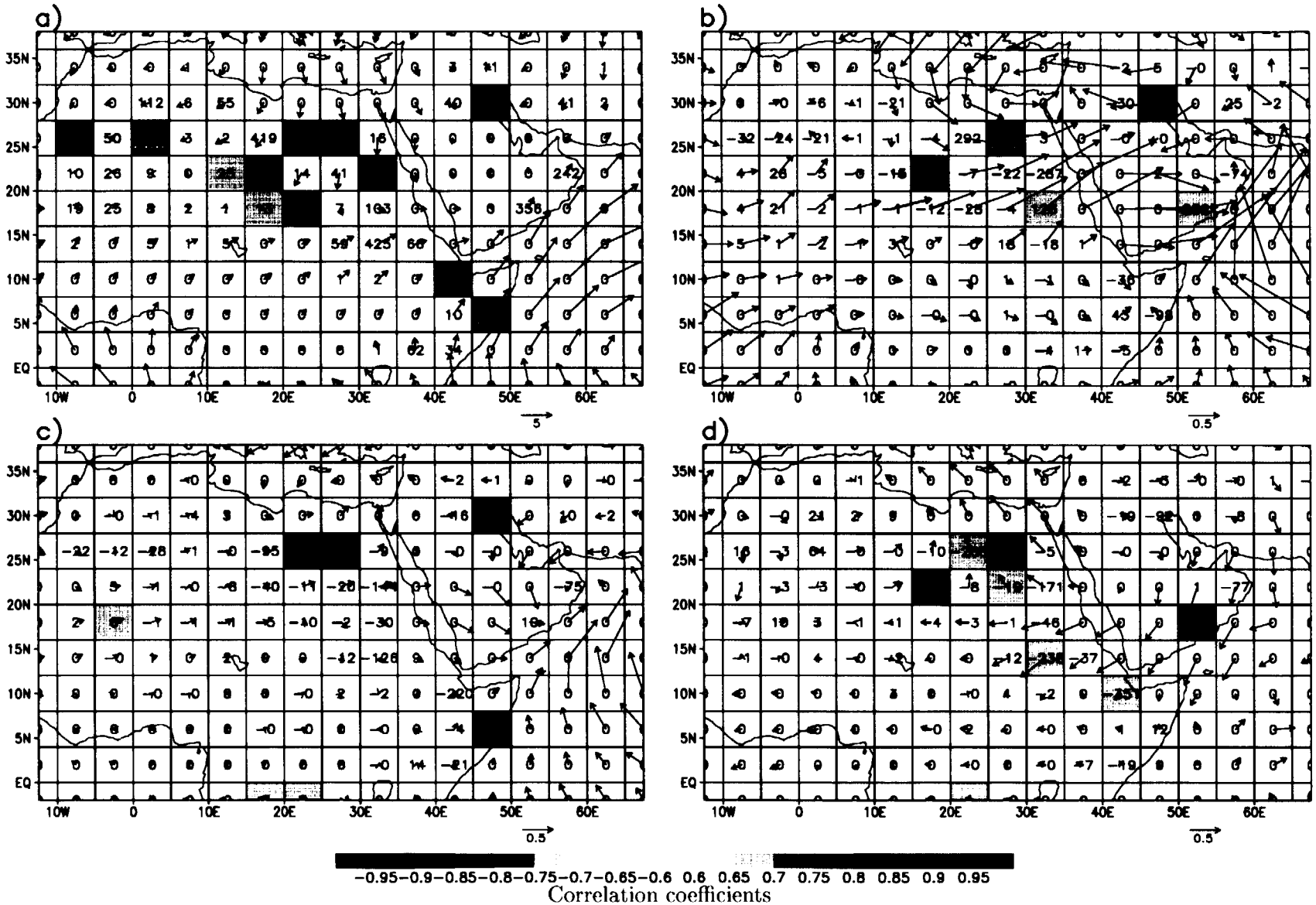
a)
b)
c)
d)
35N
30N
25N
20N
15N
10N
5N
EQ
10W
0
10E
20E
30E
40E
50E
60E
5
0.5
0.5
0.5
-0.95 -0.9 -0.85 -0.8 -0.75 -0.7 -0.65 -0.6 0.6 0.65 0.7 0.75 0.8 0.85 0.9 0.95
Correlation coefficients

Plate 2

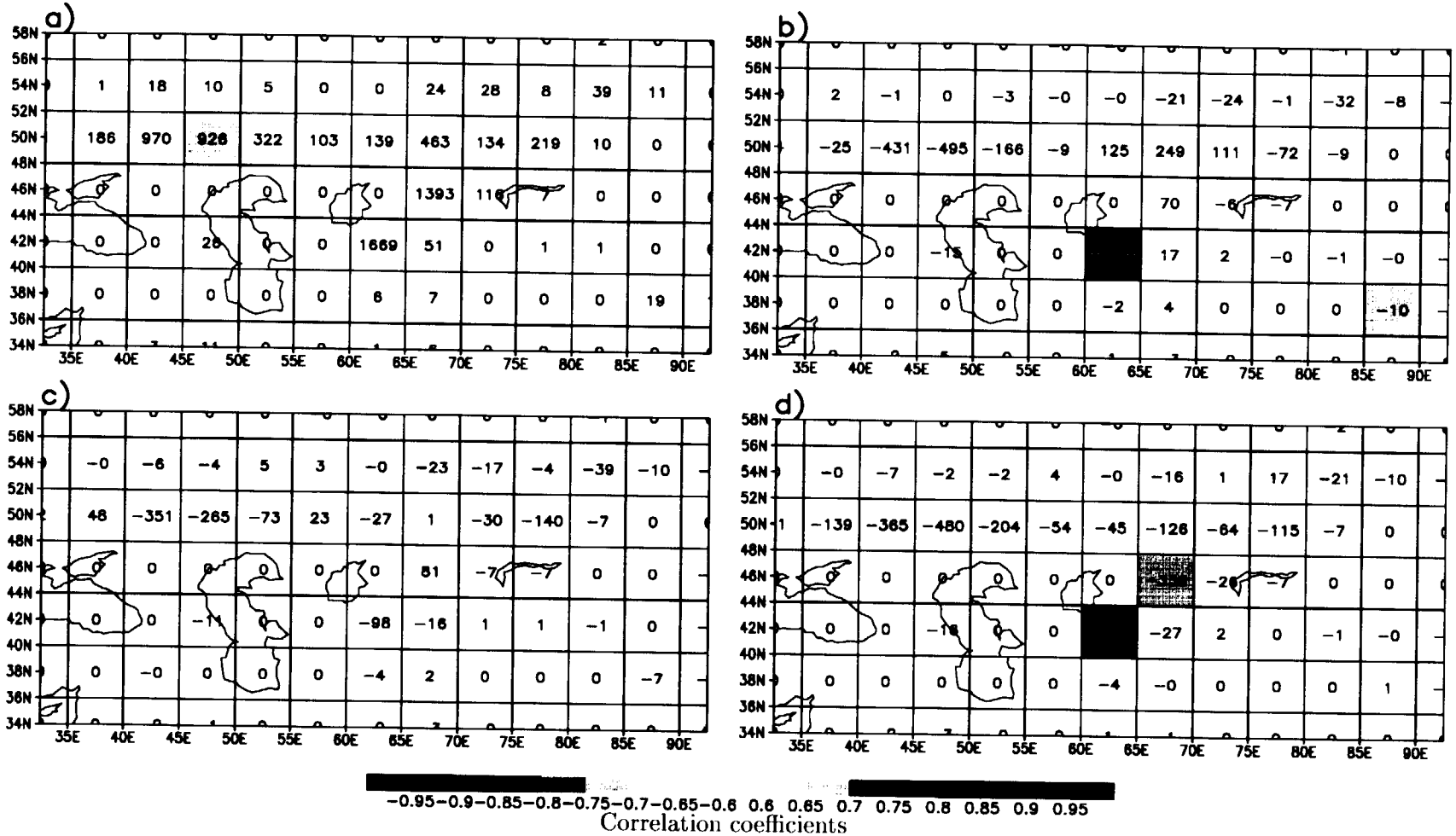
a)
b)
c)
d)
58N
56N
54N
52N
50N
48N
46N
44N
42N
40N
38N
36N
34N
35E 40E 45E 50E 55E 60E 65E 70E 75E 80E 85E 90E
-0.95 -0.9 -0.85 -0.8 -0.75 -0.7 -0.65 -0.6 0.6 0.65 0.7 0.75 0.8 0.85 0.9 0.95
Correlation coefficients

Plate 3

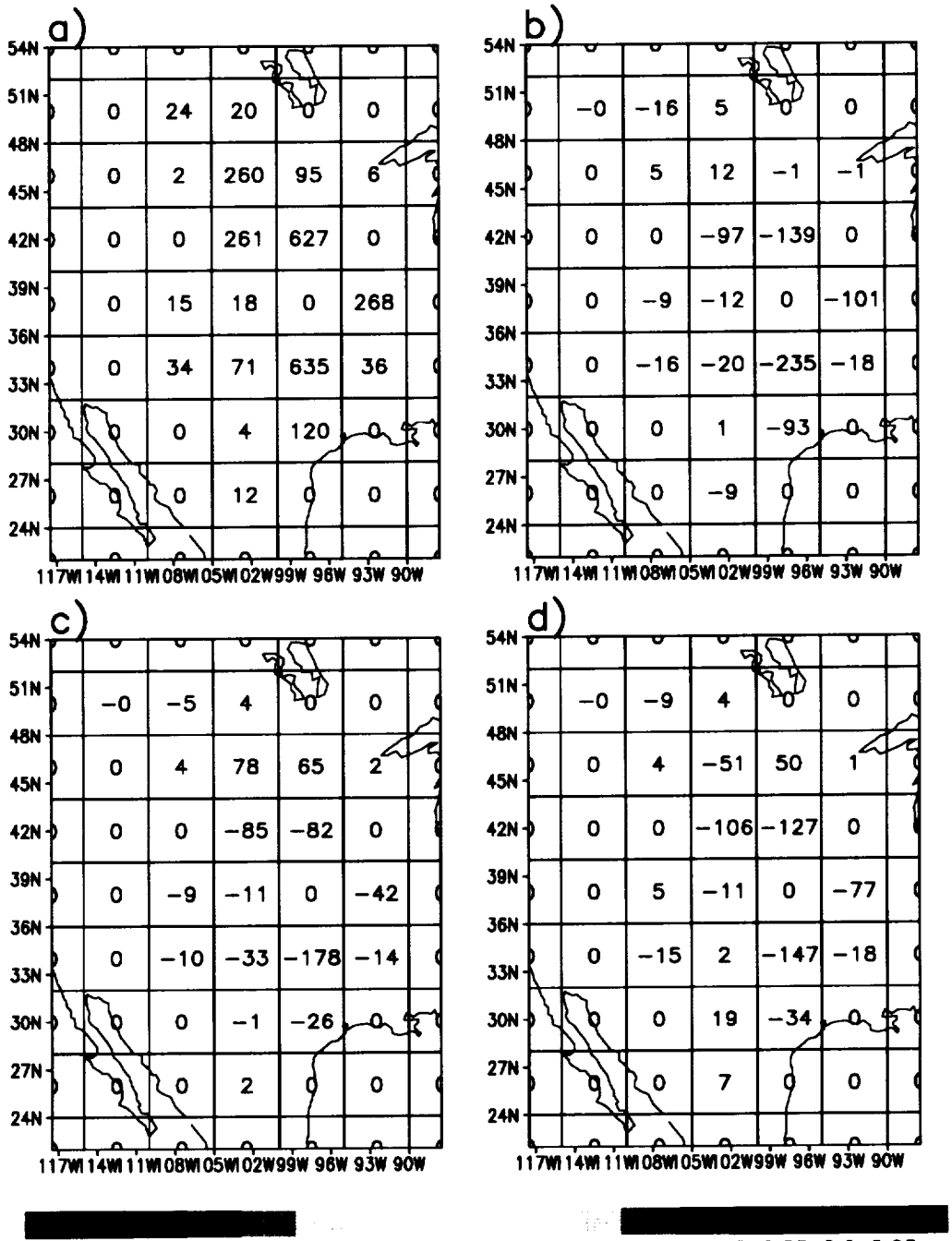
a)
54N
51N
48N
45N
42N
39N
36N
33N
30N
27N
24N
0 24 20 0 0
0 2 260 95 6
0 0 261 627 0
0 15 18 0 268
0 34 71 635 36
0 0 4 120 0
0 0 12 0 0
117W 114W 111W 108W 105W 102W 99W 96W 93W 90W
b)
54N
51N
48N
45N
42N
39N
36N
33N
30N
27N
24N
−0 −16 5 0 0
0 5 12 −1 −1
0 0 −97 −139 0
0 −9 −12 0 −101
0 −16 −20 −235 −18
0 0 1 −93 0
0 0 −9 0 0
117W 114W 111W 108W 105W 102W 99W 96W 93W 90W
c)
54N
51N
48N
45N
42N
39N
36N
33N
30N
27N
24N
−0 −5 4 0 0
0 4 78 65 2
0 0 −85 −82 0
0 −9 −11 0 −42
0 −10 −33 −178 −14
0 0 −1 −26 0
0 0 2 0 0
117W 114W 111W 108W 105W 102W 99W 96W 93W 90W
d)
54N
51N
48N
45N
42N
39N
36N
33N
30N
27N
24N
−0 −9 4 0 0
0 4 −51 50 1
0 0 −106 −127 0
0 5 −11 0 −77
0 −15 2 −147 −18
0 0 19 −34 0
0 0 7 0 0
117W 114W 111W 108W 105W 102W 99W 96W 93W 90W
−0.95 −0.9 −0.85 −0.8 −0.75 −0.7 −0.65 −0.6 0.6 0.65 0.7 0.75 0.8 0.85 0.9 0.95
Correlation coefficients

Plate 4

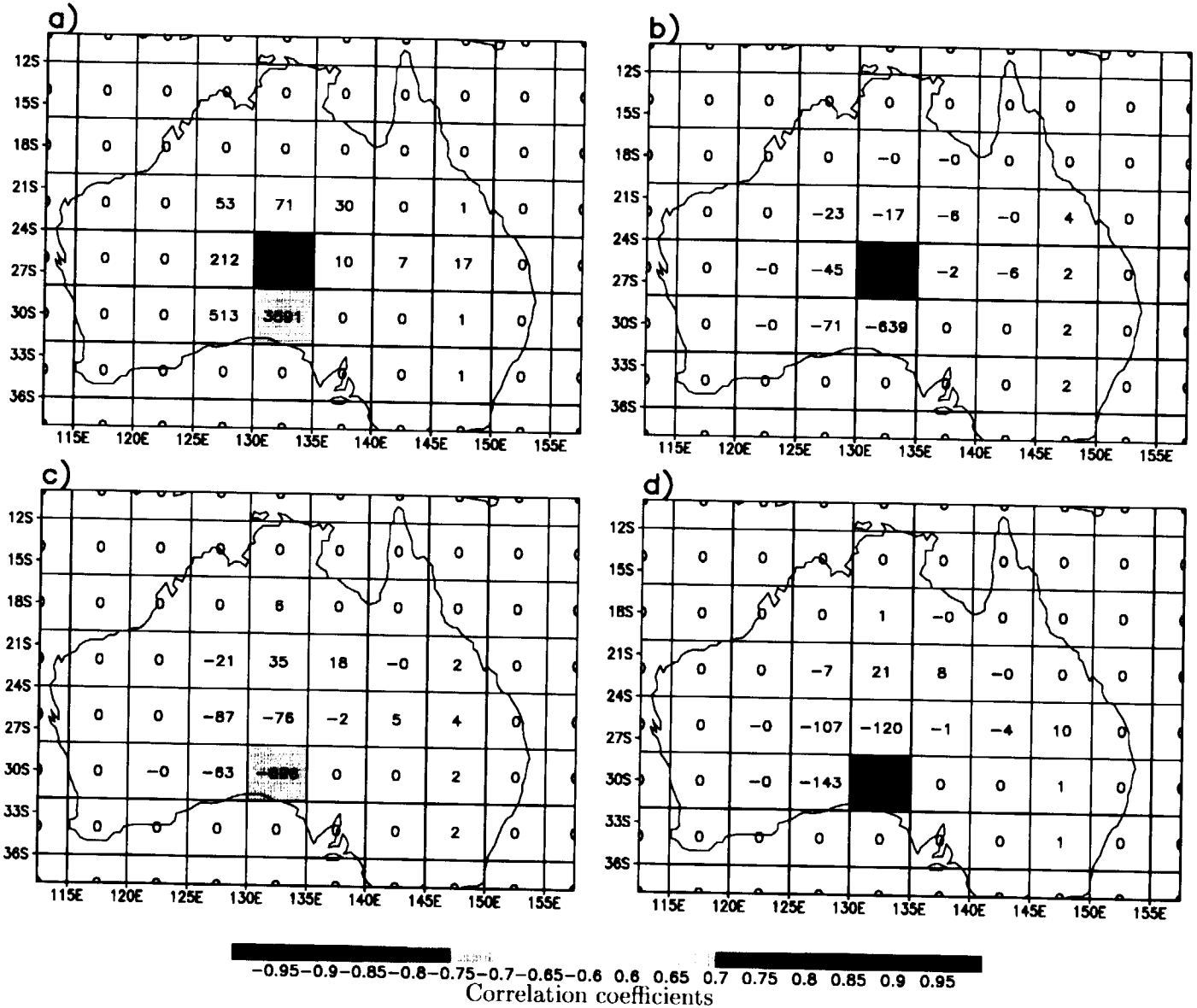
a)
b)
c)
d)
12S
15S
18S
21S
24S
27S
30S
33S
36S
115E
120E
125E
130E
135E
140E
145E
150E
155E
-0.95 -0.9 -0.85 -0.8 -0.75 -0.7 -0.65 -0.6 0.6 0.65 0.7 0.75 0.8 0.85 0.9 0.95
Correlation coefficients

Plate 5